

LRD spectral analysis of multifractional functional time series on manifolds

Diana P. Ovalle–Muñoz¹, M. Dolores Ruiz–Medina²

Abstract

This paper introduces the statistical analysis of Jacobi frequency varying Long Range Dependence (LRD) functional time series in connected and compact two–point homogeneous spaces. The convergence to zero, in the Hilbert–Schmidt operator norm, of the integrated bias of the periodogram operator is proved under alternative conditions to the ones considered in Ruiz–Medina [37]. Under this setting of conditions, weak–consistency of the minimum contrast parameter estimator of the LRD operator holds. The case where the projected manifold process can display Short Range Dependence (SRD) and LRD at different manifold scales is also analyzed. The estimation of the spectral density operator is addressed in this case. The performance of both estimation procedures is illustrated in the simulation study undertaken within the families of multifractionally integrated spherical functional autoregressive–moving average (SPHARMA) processes.

Keywords: Connected and compact two–point homogeneous spaces; Gaussian LRD multifractional functional time series; Ibragimov contrast function; multifractional in time spherical stochastic partial differential equations.

1 Introduction

The literature on weakly dependent functional time series has been widely developed in the last few decades, allowing the statistical analysis, and inference on stochastic processes under a Markovian framework (see, e.g., [3]; [20]; [21]; [22]; [23]; [24]; [27]). Nowadays, spectral analysis of functional time series models constitutes an open research area. Under suitable functional cumulant mixing conditions, and the summability in time of the trace norm of the elements of the covariance operator family, in Panaretos and Tavakoli [31],

a weighted periodogram operator estimator of the spectral density operator is derived. Its asymptotic analysis is addressed. Particularly, the asymptotic normality of the functional discrete Fourier transform (fDFT) of the curve data is proved (see also [38]). In [32], a harmonic principal component analysis of functional time series, based on Karhunen–Loève-like decomposition in the temporal functional spectral domain is proposed, the so-called Cramér–Karhunen–Loève representation (see also [35]; [36]). Some recent applications in the context of functional regression are obtained in [33]. Hypothesis testing for detecting modelling differences in functional time series dynamics is achieved in [39] in the functional spectral domain.

Recently, an attempt to extend spectral analysis of functional time series to the context of LRD functional sequences has been presented in [37], covering, in particular, some examples of the LRD functional time series family analyzed in [26] in the temporal domain. The application of harmonic analysis in this more general context entails important advantages as given in [37]. Particularly, under stationary in time, the temporal dependence range can be approximated from the behavior in a neighborhood of zero frequency of the spectral density operator family at different spatial resolution levels. Moreover, a more flexible modeling framework can be introduced in this setting, allowing the representation of long, intermediate or short range dependence, according to the interval where the pure point or continuous spectrum of the long-memory operator lies. In [26], Functional Principal Component Analysis (FPCA), based on the long-run covariance function, is applied in the consistent estimation of the dimension and the orthonormal functions spanning the dominant subspace, where the projected curve process displays the largest dependence range. Fractionally integrated autoregressive moving averages processes constitute an interesting example (see [26]). The multifractional version of this process family can be analyzed under the modeling framework introduced in [37].

Connected and compact two-point homogeneous spaces constitute an example of manifold, denoted here as \mathbb{M}_d (with d being its topological dimension), where invariance of a kernel with respect to the group of isometries of \mathbb{M}_d allows its spectral diagonalization in terms of a fixed orthogonal basis (Jacobi polynomials) of the Hilbert space $H = L^2(\mathbb{M}_d, d\nu)$. Here, $d\nu$ denotes the measure induced by the probabilistic invariant measure on the connected component of the group of isometries of \mathbb{M}_d . Particularly, this Hilbert space framework has been adopted by several authors in the current literature for the special case of the sphere, in the asymptotic analysis of functional time series (see [12]), as well as in the introduction of new model families (see [10]). Also, in the LRD framework, sphere-cross-time random fields are analyzed in [30], investigating the asymptotic behavior, under temporal

increasing domain, of the empirical measure (excursion area) at any threshold. Time-dependent random fields solution to a fractional pseudodifferential equation on the sphere are introduced in [18] (see also [5]). The discrete Jacobi polynomial transform plays a crucial role in the characterization and analysis of these random fields (see [28]). For example, Sobolev regularity and Hölder continuity of Gaussian random fields on a connected and compact two-point homogeneous space are studied in [14] and [15], by exploiting asymptotic properties of the discrete polynomial Jacobi transform. Simulation and approximation based on such a transform are illustrated in [16] and [19]. Recently, spherical multifractal models have also been introduced in [25], which are characterized via Rényi function analysis.

This paper applies the results in [37], considering the special case of $H = L^2(\mathbb{M}_d, d\nu)$. Specifically, under stationary in time and isotropy in space, Jacobi discrete frequency varying LRD functional time series models in connected and compact two-point homogeneous spaces are analyzed (see **Conditions C0–C1** below). Note that, in [37], the space of self-adjoint positive bounded linear operators is chosen to characterize, in the spectral domain, LRD in Hilbert-valued time series. Indeed, under absolute integrability of the bounded operator norms of the elements of the spectral density operator family, having one singularity at the origin, the almost surely equicontinuity of such family holds. The summability of the square of the Hilbert–Schmidt norms of the elements of the covariance operator family then follows from Parseval identity in terms of the Hilbert–Schmidt operator norm (see Lemma 1 in [37] for one singularity, that, it general holds for a finite set of singularities). This key result leads to the convergence to zero, in the Hilbert–Schmidt operator norm, of the integrated bias of the periodogram operator. Also, under some additional conditions, the weak-consistency of the minimum contrast parameter estimator of the long-memory operator is obtained.

In the present paper, **Condition C1** introduced below restricts our attention to a spectral density operator family, whose elements lie in the space of Hilbert–Schmidt operators, except for the element at zero frequency. Particularly, the Hilbert–Schmidt operator norms of the elements of such a family define a square integrable function on the interval $[-\pi, \pi]$. Under this scenario, the convergence to zero of the integrated bias of the periodogram operator in the Hilbert–Schmidt operator norm can be obtained in a simpler way than in [37] (see Theorem 1 below). The weak-consistency of the minimum contrast parameter estimator of the long-memory operator then follows in a similar way to Theorem 2 in [37]. This more restrictive spectral density operator family still allows to model LRD. On the other hand, the space of Hilbert–Schmidt operators on a separable Hilbert space H is a

usual parametric space in functional time series analysis under a state space framework (see, e.g., [9]). That is the case of SPHARMA processes, and, in particular, of SPHAR processes, whose isotropic kernels involved in the autoregression are often assumed to be in the space of Hilbert–Schmidt operators on $L^2(\mathbb{S}_2, d\nu)$, with $d\nu$ denoting the uniform measure on the sphere \mathbb{S}_2 in \mathbb{R}^3 (see, e.g., Condition 14 and Remark 15 in [12]).

Finally, we analyze the case of functional time series displaying Short Range Dependence (SRD) and LRD at different manifold scales. In that scenario we combine a semiparametric estimation of the spectral density operator, based on minimum contrast, at manifold scales where LRD is displayed, and a nonparametric estimation, based on the weighted periodogram operator, in the remaining manifold scales where SRD is observed (see Section 4). The performance of the estimation approaches analyzed is illustrated in the simulation study undertaken in the context of multifractionally integrated SPHARMA processes. Specifically, a multifractionally integrated SPHAR(3) process is generated, whose LRD operator has eigenvalues lying in the interval (a, b) , with $0 < a < b < 1$. The special case of an increasing sequence of eigenvalues is considered. The temporal persistence is stronger at small spherical scales than at large scales, since, in this numerical example, the eigenvalues of the LRD operator are very close to zero at low discrete Legendre frequencies. In the second scenario where SRD and LRD are displayed by the projected spherical process at different Legendre frequencies, a multifractionally integrated SPHARMA(1,1) process is generated. The eigenvalues of the LRD operator are null at a countable set of Legendre frequencies, leading to a SRD behavior of the corresponding projected process. Particularly, under this scenario, SRD at high Legendre frequencies, and LRD at low frequency is displayed. The proposed mixed (parametric/nonparametric) estimation methodology is implemented under this setting to illustrate its performance, in the approximation of memory in time depending on the manifold scale.

The outline of the paper is the following. Section 2 provides preliminary results on connected and compact two-point homogeneous spaces. The minimum contrast parameter estimation methodology is introduced in Section 3, in an infinite-dimensional framework, providing some asymptotic results in the spectral domain. An extended formulation of this estimation methodology to the case where temporal LRD and SRD are displayed at different manifold scales is proposed in Section 4. A simulation study is undertaken in Section 5 to illustrate the performance of the proposed estimation methodologies of the spectral density operator under LRD, and LRD–SRD. Final comments in Section 6 end the paper.

2 Preliminaries

We review here some of the results derived in [28] on Karhunen–Loève–like representation of second–order mean–square continuous elliptically contoured random fields on a manifold \mathbb{M}_d , under stationary in time and isotropic in space, in the context of connected and compact two–point homogeneous spaces.

Let $X = \{X(\mathbf{x}, t), \mathbf{x} \in \mathbb{M}_d, t \in \mathbb{T}\}$ be a wide sense stationary in time and isotropic in space zero–mean, and mean–square continuous random field on the basic probability space (Ω, \mathcal{A}, P) . Here, \mathbb{T} denotes the temporal domain which is assumed to be \mathbb{R} , the real numbers, or \mathbb{Z} , the integer numbers. Assume also that the map $\tilde{X}_t : (\Omega, \mathcal{A}) \rightarrow (L^2(\mathbb{M}_d, d\nu), \mathcal{B}(L^2(\mathbb{M}_d, d\nu)))$ is measurable, with $\tilde{X}_t(\mathbf{x}) := X(\mathbf{x}, t)$ for every $t \in \mathbb{T}$ and $\mathbf{x} \in \mathbb{M}_d$. Here, $\mathcal{B}(L^2(\mathbb{M}_d, d\nu))$ denotes the σ –algebra generated by all cylindrical subsets of $L^2(\mathbb{M}_d, d\nu)$. The stationary and isotropic kernel C defining the covariance function of random field X is then given by

$$C(d_{\mathbb{M}_d}(\mathbf{x}, \mathbf{y}), t - s) = E[X(\mathbf{x}, t)X(\mathbf{y}, s)], \mathbf{x}, \mathbf{y} \in \mathbb{M}_d, t, s \in \mathbb{T}, \quad (1)$$

where $d_{\mathbb{M}_d}$ denotes here the geodesic distance induced by the isometry with the sphere, preserving the spherical distance $\rho(\mathbf{x}, \mathbf{y}) = \cos^{-1}(\mathbf{x}, \mathbf{y})$, for every $\mathbf{x}, \mathbf{y} \in \mathbb{S}_d$ (see, e.g., [28] for more details).

Under conditions of Theorems 4 in [28], i.e., $\sum_{n=0}^{\infty} B_n(0)P_n^{(\alpha, \beta)}(1)$ converges, and $C(d_{\mathbb{M}_d}(\mathbf{x}, \mathbf{y}), t) = C(d_{\mathbb{M}_d}(\mathbf{x}, \mathbf{y}), -t)$, the following diagonal series expansion is admitted by C , in terms of Jacobi polynomials $P_n^{(\alpha, \beta)}$, depending on parameter vector (α, β) (see, e.g., [4]):

$$C(d_{\mathbb{M}_d}(\mathbf{x}, \mathbf{y}), t - s) = \sum_{n=0}^{\infty} B_n(t - s)P_n^{(\alpha, \beta)}(\cos(d_{\mathbb{M}_d}(\mathbf{x}, \mathbf{y}))), \mathbf{x}, \mathbf{y} \in \mathbb{M}_d, t, s \in \mathbb{T}. \quad (2)$$

Theorem 5 in [28] then leads to the following orthogonal expansion of X :

$$X(\mathbf{x}, t) = \sum_{n=0}^{\infty} V_n(t)P_n^{(\alpha, \beta)}(\cos(d_{\mathbb{M}_d}(\mathbf{x}, \mathbf{U}))), \mathbf{x} \in \mathbb{M}_d, t \in \mathbb{T}, \quad (3)$$

where $\{V_n(t), t \in \mathbb{T}, n \in \mathbb{N}_0\}$ is a sequence of independent stationary centered random processes on \mathbb{T} . Thus, $E[V_n(t)] = 0$, and for $m \neq n$, and for every $t \in \mathbb{T}$, and $\mathbf{z} \in \mathbb{M}_d$,

$$\text{cov}(V_n(t)P_n^{(\alpha, \beta)}(\cos(d_{\mathbb{M}_d}(\mathbf{z}, \mathbf{U}))), V_m(t)P_m^{(\alpha, \beta)}(\cos(d_{\mathbb{M}_d}(\mathbf{z}, \mathbf{U})))) = 0,$$

with, for $n \in \mathbb{N}_0$, $E[V_n(t)V_n(s)] = a_n^2 B_n(t-s)$. Here, the sequence $\{a_n, n \in \mathbb{N}_0\}$ is given by (see Lemma 2 in [28]):

$$a_n = \left[\frac{\Gamma(\beta+1)(2n+\alpha+\beta+1)\Gamma(n+\alpha+\beta+1)}{\Gamma(\alpha+\beta+2)\Gamma(n+\beta+1)} \right]^{1/2}, \quad n \in \mathbb{N}_0.$$

The random variable \mathbf{U} is uniformly distributed on \mathbb{M}_d , and is independent of $\{V_n(t), n \in \mathbb{N}_0\}$.

In the subsequent development, we will consider $\mathbb{T} = \mathbb{Z}$. Under the conditions assumed, from equation (3), we will work under the umbrella of second-order $L^2(\mathbb{M}_d, d\nu)$ -valued time series. That is, the following assumption is made:

Condition C0. The sequence of stationary covariance functions $\{B_n, n \in \mathbb{N}_0\}$ in equation (2) is such that

$$\sum_{n \in \mathbb{N}_0} |B_n(0)| = \sum_{n \in \mathbb{N}_0} B_n(0) < \infty,$$

which is equivalent to the trace property of the autocovariance operator $\mathcal{R}_0 = E[\tilde{X}_t \otimes \tilde{X}_t] = E[\tilde{X}_0 \otimes \tilde{X}_0]$, for every $t \in \mathbb{Z}$, of \tilde{X} .

Remark 1 Note that under **Condition C0**, applying Cauchy-Schwarz inequality, and stationarity of covariance function B_n , for every $n \in \mathbb{N}_0$, we have for each $t \in \mathbb{Z}$,

$$\sum_{n \in \mathbb{N}_0} |B_n(t)| \leq \sum_{n \in \mathbb{N}_0} |B_n(0)| < \infty.$$

Furthermore, denoting, for every $\omega \in [-\pi, \pi]$, and $n \in \mathbb{N}_0$,

$$f_n(\omega) = \sum_{t \in \mathbb{Z}} \exp(-i\omega t) B_n(t)$$

(see also Section 2.2 in [29])

$$\frac{1}{2\pi} \sum_{n \in \mathbb{N}_0} \int_{-\pi}^{\pi} f_n(\omega) d\omega = \sum_{n \in \mathbb{N}_0} B_n(0) = \|\mathcal{R}_0\|_{L^1(L^2(\mathbb{M}_d, d\nu))} < \infty, \quad (4)$$

where $\|\cdot\|_{L^1(L^2(\mathbb{M}_d, d\nu))}$ denotes the norm in the space of nuclear or trace operators on $L^2(\mathbb{M}_d, d\nu)$.

Particularly, under **Condition C0**, for every $\mathbf{x} \in \mathbb{M}_d$, and for each $t \in \mathbb{Z}$, $\tilde{X}_t(\mathbf{x}) = X(\mathbf{x}, t)$ defines a second-order $L^2(\mathbb{M}_d, d\nu)$ -valued functional time series (see, e.g., Section 1 in Chapter 1 in [9]). We then address the statistical analysis of $X = \{X(\mathbf{x}, t), \mathbf{x} \in \mathbb{M}_d, t \in \mathbb{T}\}$, from a functional sample of size T $\{\tilde{X}_t, t = 1, \dots, T\}$ of correlated in time $L^2(\mathbb{M}_d, d\nu)$ -valued observations.

Remark 2 *Note that, under the above setting of conditions, Example 2 in Section 3.4 in [37] (see also [17] about related aliasing effects arising in the associated discrete sampling) allows the extension of the presented approach to the framework of spatiotemporal random fields in continuous space and time, including the special case of the Gaussian spatiotemporal random field solution of multifractional in time and fractional in space stochastic partial pseudodifferential equations (see, e.g., [6]; [7], for the case of fractional in time and fractional/multifractional in space stochastic partial pseudodifferential equations on regular bounded domains).*

3 Operator based minimum contrast parameter estimation of LRD

Let, for $\omega \in [-\pi, \pi] \setminus \{0\}$, \mathcal{F}_ω be the spectral density operator (see [37]):

$$\mathcal{F}_\omega \underset{\mathcal{L}(L^2(\mathbb{M}_d, d\nu; \mathbb{C}))}{=} \frac{1}{2\pi} \sum_{t \in \mathbb{Z}} \exp(-i\omega t) \mathcal{R}_t, \quad (5)$$

where $\mathcal{L}(L^2(\mathbb{M}_d, d\nu; \mathbb{C}))$ denotes the space of bounded linear operators on $L^2(\mathbb{M}_d, d\nu; \mathbb{C})$. In our subsequent development, we will adopt the following LRD functional time series framework:

Condition C1. The elements of the sequence of Fourier transforms $\{f_n, n \in \mathbb{N}_0\}$ in Remark 1 admit the following semiparametric modeling:

$$f_{n,\theta}(\omega) = B_n^\eta(0) M_n(\omega) [4(\sin(\omega/2))^2]^{-\alpha(n,\theta)/2}, \quad \theta \in \Theta, \quad n \in \mathbb{N}_0, \quad (6)$$

for every $\omega \in [-\pi, \pi] \setminus \{0\}$, with, for $n \in \mathbb{N}_0$, $B_n^\eta(0) \geq 0$ being such that $\sum_{n \in \mathbb{N}_0} B_n^\eta(0) < \infty$ (see, e.g., Section 3.3, Example 1, equation (3.21), where such a sequence defines the eigenvalues of the autocovariance operator of the innovation process). Here $l_\alpha(\theta) \leq \alpha(n, \theta) \leq L_\alpha(\theta)$, for any $n \geq 0$, and $\theta \in \Theta$, for certain $l_\alpha(\theta), L_\alpha(\theta) \in (0, 1/2)$, where Θ denotes a compact parameter space with non null interior. For each $\theta \in \Theta$, the sequence $\{\alpha(n, \theta), n \geq 0\}$

defines the series expansion of the parameterized long-memory operator \mathcal{A}_θ with kernel $\mathcal{K}_{\mathcal{A}_\theta}$ given by:

$$\mathcal{K}_{\mathcal{A}_\theta}(\mathbf{x}, \mathbf{y}) = \sum_{n \in \mathbb{N}_0} \alpha(n, \theta) P_n^{(\alpha, \beta)}(\cos(d_{\mathbb{M}_d}(\mathbf{x}, \mathbf{y}))), \quad \mathbf{x}, \mathbf{y} \in \mathbb{M}_d.$$

That is, for every $\theta \in \Theta$, \mathcal{A}_θ has isotropic kernel and defines a strictly positive self-adjoint operator on $L^2(\mathbb{M}_d, d\nu)$ with $\mathcal{L}(L^2(\mathbb{M}_d, d\nu))$ -norm less than $1/2$. It is also assumed that, for every $n \in \mathbb{N}_0$, $M_n(\cdot)$ defines a slowly varying function at $\omega = 0$ in the Zygmund's sense (see, e.g., Definition 6.6 in [8]). Furthermore, for each $\omega \in [-\pi, \pi]$, $\{M_n(\omega), n \in \mathbb{N}_0\}$ are the eigenvalues of operator $\mathcal{M}_\omega \in \mathcal{S}(L^2(\mathbb{M}_d, d\nu; \mathbb{C}))$, the space of Hilbert-Schmidt operators on $L^2(\mathbb{M}_d, d\nu; \mathbb{C})$, and $\|\mathcal{M}_\omega\|_{\mathcal{S}(L^2(\mathbb{M}_d, d\nu; \mathbb{C}))} \in L^2([-\pi, \pi])$. The nonparametric operator family $\{\mathcal{M}_\omega, \omega \in [-\pi, \pi]\}$ models the regular spectrum representing a Markovian modelling. The elements of the associated kernel family are given by

$$\mathcal{K}_{\mathcal{M}_\omega}(\mathbf{x}, \mathbf{y}) = \sum_{n \in \mathbb{N}_0} M_n(\omega) P_n^{(\alpha, \beta)}(\cos(d_{\mathbb{M}_d}(\mathbf{x}, \mathbf{y}))), \quad \mathbf{x}, \mathbf{y} \in \mathbb{M}_d, \quad \omega \in [-\pi, \pi].$$

Remark 3 Under **Condition C1**, the eigenvalues of the long-memory operator are in the interval $(0, 1/2)$. Hence, a weaker range of singularity (or unboundedness) at zero frequency is considered, but it still allows to model LRD in functional time series. Note also that Lemma 1 in [37] is derived under $\int_{-\pi}^{\pi} \|\mathcal{F}_\omega\|_{\mathcal{L}(\tilde{H})} d\omega < \infty$, leading to the almost surely equicontinuity of $\{\mathcal{F}_\omega, \omega \in [-\pi, \pi]\}$. In that paper, equicontinuity holds except for the element \mathcal{F}_0 which does not belong to $\mathcal{L}(L^2(\mathbb{M}_d, d\nu; \mathbb{C}))$.

Under **Conditions C0–C1**, the kernel $f_\omega(\mathbf{x}, \mathbf{y})$ of the spectral density operator \mathcal{F}_ω admits the following series expansion in the space $L^2(\mathbb{M}_d \times \mathbb{M}_d, d\nu \otimes d\nu)$, and hence, in the space $\mathcal{L}(L^2(\mathbb{M}_d, d\nu))$: For $\omega \in [-\pi, \pi] \setminus \{0\}$,

$$f_\omega(\mathbf{x}, \mathbf{y}) = \sum_{n=0}^{\infty} \frac{1}{2\pi} \left[\sum_{t \in \mathbb{T}} \exp(-i\omega t) B_n(t) \right] P_n^{(\alpha, \beta)}(\cos(d_{\mathbb{M}_d}(\mathbf{x}, \mathbf{y}))), \quad \mathbf{x}, \mathbf{y} \in \mathbb{M}_d. \quad (7)$$

Equivalently, for every $n \geq 0$, and $\omega \in [-\pi, \pi] \setminus \{0\}$, denoting

$$\tilde{f}_n(\omega) := \frac{1}{2\pi} \left[\sum_{t \in \mathbb{T}} \exp(-i\omega t) B_n(t) / (\dim(H_n)) \right],$$

one can write

$$f_\omega(\mathbf{x}, \mathbf{y}) = \sum_{n=0}^{\infty} \frac{\dim(H_n)}{4\pi} \tilde{f}_n(\omega) P_n^{(\alpha, \beta)}(\cos(d_{\mathbb{M}_d}(\mathbf{x}, \mathbf{y}))), \quad \mathbf{x}, \mathbf{y} \in \mathbb{M}_d, \quad (8)$$

where, for each $t \in \mathbb{Z}$, $\{C_n(t) = B_n(t)/(\dim(H_n)), n \in \mathbb{N}_0\}$ can be interpreted as the time-varying angular power spectrum of spatiotemporal random field X , which is usually analyzed in Cosmic Microwave Background (CMB) applications involved in the special case of the sphere (see [29]; [30]; [28]). Here, for each $n \in \mathbb{N}_0$, $\dim(H_n)$ is the dimension of the eigenspace associated with the eigenvalue $\lambda_n = -n\varepsilon(n\varepsilon + \alpha + \beta + 1)$ of the Laplace–Beltrami operator on $L^2(\mathbb{M}_d, d\nu)$, i.e.,

$$\dim(H_n) = \frac{(2n + \alpha' + \beta + 1)\Gamma(\beta + 1)\Gamma(n + \alpha + \beta + 1)\Gamma(n + \alpha + 1)}{\Gamma(\alpha + 1)\Gamma(\alpha + \beta + 2)\Gamma(n + 1)\Gamma(n + \beta + 1)}.$$

Note that, $\alpha = (p + q - 1)/2$, $\beta = (q - 1)/2$, and $\varepsilon = 2$ if $\mathbb{M}_d = \mathbb{P}^d(\mathbb{R})$, the projective space over the field \mathbb{R} , and $\varepsilon = 1$, otherwise. Parameters q and p are the dimensions of some root spaces connected with the Lie algebras of the groups G and K , with $\mathbb{M}_d \simeq G/K$, being G the connected component of the group of isometries of \mathbb{M}_d , and K the stationary subgroup of a fixed point \mathbf{o} in \mathbb{M}_d (see, e.g., Table 1 in [28], providing an exhaust list of compact connected two-point homogeneous spaces, displaying, in particular, their respective q and p parameter values, and see also [13], for more details on Lie Algebra based approach).

From (8), the following Cramér–Karhunen–Loève representation for the second-order mean-square continuous elliptically contoured random field X on \mathbb{M}_d then holds: For $\mathbf{x} \in \mathbb{M}_d$, and $t \in \mathbb{Z}$,

$$\tilde{X}_t(\mathbf{x}) = X(\mathbf{x}, t) = \sum_{n=0}^{\infty} \left[\int_{-\pi}^{\pi} \exp(i\omega t) dZ_n(\omega) \right] P_n^{(\alpha, \beta)}(\cos(d_{\mathbb{M}_d}(\mathbf{x}, \mathbf{U}))), \quad (9)$$

where, for $\omega \in [-\pi, \pi]$, $Z_n(\omega)$ is the n th projection $\left\langle Z(\omega), P_n^{(\alpha, \beta)} \right\rangle_{L^2(\mathbb{M}_d, d\nu; \mathbb{C})}$, $n \geq 0$, of a random element $Z(\omega) \in L^2(\mathbb{M}_d, d\nu; \mathbb{C})$, with $E \|Z(\omega)\|_{L^2(\mathbb{M}_d, d\nu; \mathbb{C})}^2 = \sum_{l=0}^{\infty} \frac{\dim(H_l)}{4\pi} \int_{-\pi}^{\omega} \tilde{f}_l(\omega) d\omega$. The infinite-dimensional process $\{Z(\omega), \omega \in [-\pi, \pi]\}$ has orthogonal increments, i.e., for $\omega_1 > \omega_2 \geq \omega_3 > \omega_4$,

$$E \langle Z(\omega_1) - Z(\omega_2), Z(\omega_3) - Z(\omega_4) \rangle_{L^2(\mathbb{M}_d, d\nu; \mathbb{C})} = 0.$$

Hence, for $\omega \in [-\pi, \pi]$,

$$E [Z_n(\omega) Z_m(\tilde{\omega})] = \delta_{n,m} \left[\int_{-\pi}^{\min(\omega, \tilde{\omega})} \tilde{f}_n(\omega) d\omega \right].$$

Note that, for $\mathbf{x} \in \mathbb{M}_d$, and $t \in \mathbb{Z}$,

$$\begin{aligned} & E \left| X_t(\mathbf{x}) - \sum_{n=0}^M \left[\int_{-\pi}^{\pi} \exp(i\omega t) dZ_n(\omega) \right] P_n^{(\alpha, \beta)}(\cos(d_{\mathbb{M}_d}(\mathbf{x}, \mathbf{U})) \right|^2 \\ &= \sum_{n>M} \left(\frac{\dim(H_n)}{4\pi} \right) \int_{-\pi}^{\pi} \tilde{f}_n(\omega) d\omega, \end{aligned} \quad (10)$$

in the $L^2(\mathbb{M}_d, d\nu)$ sense.

3.1 Estimation under a semiparametric model

This section addresses the minimum contrast parameter estimation of the long-memory operator \mathcal{A}_θ characterizing the large scale behavior in time of the family of LRD functional sequences introduced in **Condition C1**. Under **Conditions C0–C1**, the convergence to zero in the Hilbert–Schmidt operator norm of the integrated bias of the periodogram operator holds (see Theorem 1 below). The weak-consistency of the minimum contrast parameter estimator of the long-memory operator then follows in the Gaussian case as given in Theorem 2.

Theorem 1 *Under Conditions C0–C1,*

$$\left\| \int_{-\pi}^{\pi} [\mathcal{F}_\omega - \mathcal{F}_\omega^{(T)}] d\omega \right\|_{\mathcal{S}(L^2(\mathbb{M}_d, d\nu; \mathbb{C}))} \rightarrow 0, \quad T \rightarrow \infty,$$

where $\mathcal{F}_\omega^{(T)}$ denotes the mean of the periodogram operator

$$p_\omega^{(T)} = \tilde{X}_\omega^{(T)} \otimes \overline{\tilde{X}_\omega^{(T)}}, \quad \omega \in [-\pi, \pi],$$

and

$$\tilde{X}_\omega^{(T)}(\cdot) \underset{L^2(\mathbb{M}_d, d\nu; \mathbb{C})}{=} \frac{1}{\sqrt{2\pi T}} \sum_{t=1}^T X_t(\cdot) \exp(-i\omega t), \quad \omega \in [-\pi, \pi], \quad (11)$$

denotes the *fDFT*. Here, as before, $\|\cdot\|_{\mathcal{S}(L^2(\mathbb{M}_d, d\nu; \mathbb{C}))}$ is the norm in the space $\mathcal{S}(L^2(\mathbb{M}_d, d\nu; \mathbb{C}))$ of Hilbert–Schmidt operators on $L^2(\mathbb{M}_d, d\nu; \mathbb{C})$.

Proof. Under **Condition C1**,

$$\begin{aligned} & \int_{-\pi}^{\pi} \|\mathcal{F}_\omega\|_{\mathcal{S}(L^2(\mathbb{M}_d, d\nu; \mathbb{C}))}^2 d\omega = \sum_{n \in \mathbb{N}_0} \int_{-\pi}^{\pi} |f_n(\omega)|^2 d\omega \\ & \leq \left\{ \left[\int_{-\pi}^{-1} + \int_1^{\pi} \right] |\omega|^{-2L(\theta)} + \int_{-1}^1 |\omega|^{-2l(\theta)} \right\} \|\mathcal{M}_\omega\|_{\mathcal{S}(L^2(\mathbb{M}_d, d\nu; \mathbb{C}))}^2 d\omega < \infty. \end{aligned} \quad (12)$$

Note that applying Parseval identity, we also have

$$\sum_{t \in \mathbb{Z}} \|\mathcal{R}_t\|_{\mathcal{S}(L^2(\mathbb{M}_d, d\nu))}^2 = \int_{-\pi}^{\pi} \|\mathcal{F}_\omega\|_{\mathcal{S}(L^2(\mathbb{M}_d, d\nu; \mathbb{C}))}^2 d\omega < \infty.$$

Finally, from (12), equations (4.6)–(4.8) in the proof of Theorem 1 in [37] follow. The rest of the proof of this result can then be derived in a similar way to Theorem 1 in [37], keeping in mind that from (12),

$$\int_{-\pi}^{\pi} \|\mathcal{F}_\omega\|_{\mathcal{L}(L^2(\mathbb{M}_d, d\nu; \mathbb{C}))}^2 d\omega \leq \int_{-\pi}^{\pi} \|\mathcal{F}_\omega\|_{\mathcal{S}(L^2(\mathbb{M}_d, d\nu; \mathbb{C}))}^2 d\omega < \infty.$$

3.2 Minimum contrast parameter estimation

Assume that the true parameter value θ_0 lies in the interior of Θ , a compact set with non empty interior, denoted as $\text{int } \Theta$. The parametric sequence of eigenvalues $\{\alpha(n, \theta), n \geq 0, \theta \in \Theta\}$ satisfies $\alpha(\cdot, \theta_1) \neq \alpha(\cdot, \theta_2)$, for $\theta_1 \neq \theta_2$, and $\theta_1, \theta_2 \in \Theta$. The elements involved in the computation of the minimum contrast estimator $\hat{\theta}_T$, based on a functional sample of size T , are now introduced. Particularly, we denote by $\{\hat{\alpha}_T(n, \theta) = \alpha(n, \hat{\theta}_T), n \in \mathbb{N}_0\}$ the resulting parametric estimators of the eigenvalues of \mathcal{A}_θ .

In the definition of our loss function, integration in the temporal spectral domain with respect to a suitable weighting operator \mathcal{W}_ω is achieved. The operator integrals are understood here as improper operator Stieltjes integrals which converge strongly (see, e.g., Section 8.2.1 in [34]). For each $\omega \in [-\pi, \pi]$, our weighting operator \mathcal{W}_ω has isotropic kernel on $\mathbb{M}_d \times \mathbb{M}_d$ given by

$$\begin{aligned} \mathcal{K}_{\mathcal{W}_\omega}(\mathbf{x}, \mathbf{y}) &= \sum_{n \geq 0} W(\omega, n, \gamma) P_n^{(\alpha, \beta)}(\cos(d_{\mathbb{M}_d}(\mathbf{x}, \mathbf{y}))) \\ &= \sum_{n \geq 0} \widetilde{W}(n) |\omega|^\gamma P_n^{(\alpha, \beta)}(\cos(d_{\mathbb{M}_d}(\mathbf{x}, \mathbf{y}))), \quad \gamma > 0, \quad \mathbf{x}, \mathbf{y} \in \mathbb{M}_d. \end{aligned} \tag{13}$$

Its eigenvalues $\{W(\omega, n, \gamma) = \widetilde{W}(n) |\omega|^\gamma, n \in \mathbb{N}_0\}$ satisfy the conditions assumed in Section 5 and Theorem 2 in [37]. Particularly, the eigenvalues $\{\widetilde{W}(n), n \in \mathbb{N}_0\}$ of operator $\widetilde{\mathcal{W}} \in \mathcal{L}(L^2(\mathbb{M}_d, d\nu; \mathbb{C}))$ are such that

$$\begin{aligned} 0 < m_{\widetilde{\mathcal{W}}} &= \inf_{\psi \in L^2(\mathbb{M}_d, d\nu; \mathbb{C}); \|\psi\|_{L^2(\mathbb{M}_d, d\nu; \mathbb{C})} = 1} \left\langle \widetilde{\mathcal{W}}(\psi), \psi \right\rangle_{L^2(\mathbb{M}_d, d\nu; \mathbb{C})}, \\ 0 < M_{\widetilde{\mathcal{W}}} &= \sup_{\psi \in L^2(\mathbb{M}_d, d\nu; \mathbb{C}); \|\psi\|_{L^2(\mathbb{M}_d, d\nu; \mathbb{C})} = 1} \left\langle \widetilde{\mathcal{W}}(\psi), \psi \right\rangle_{L^2(\mathbb{M}_d, d\nu; \mathbb{C})}. \end{aligned} \tag{14}$$

Under **Condition C1**, for each $\theta \in \Theta$, the kernel $\mathcal{K}_{\sigma_\theta^2}$ of the normalizing operator σ_θ^2 is computed as follows: For every $\mathbf{x}, \mathbf{y} \in \mathbb{M}_d$,

$$\begin{aligned}\mathcal{K}_{\sigma_\theta^2}(\mathbf{x}, \mathbf{y}) &= \sum_{n \geq 0} \widetilde{W}(n) \left[\int_{-\pi}^{\pi} f_{n,\theta}(\omega) |\omega|^\gamma d\omega \right] P_n^{(\alpha,\beta)}(\cos(d_{\mathbb{M}_d}(\mathbf{x}, \mathbf{y}))) \\ &= \sum_{n \geq 0} \widetilde{W}(n) \left[\int_{-\pi}^{\pi} \frac{B_n^\eta(0) M_n(\omega) [4(\sin(\omega/2))^2]^{-\alpha(n,\theta)/2}}{|\omega|^{-\gamma}} d\omega \right] \\ &\quad \times P_n^{(\alpha,\beta)}(\cos(d_{\mathbb{M}_d}(\mathbf{x}, \mathbf{y}))).\end{aligned}\tag{15}$$

Thus, the pure point spectrum $\{\Sigma_\theta^2(n), n \geq 0\}$ of σ_θ^2 is given by

$$\Sigma_\theta^2(n) = \widetilde{W}(n) \int_{-\pi}^{\pi} \frac{B_n^\eta(0) M_n(\omega) [4(\sin(\omega/2))^2]^{-\alpha(n,\theta)/2}}{|\omega|^{-\gamma}} d\omega, \quad n \geq 0.\tag{16}$$

For $(\omega, \theta) \in [-\pi, \pi] \setminus \{0\} \times \Theta$, the spectral density operator $\mathcal{F}_{\omega,\theta}$ then admits the following factorization:

$$\mathcal{F}_{\omega,\theta} = \sigma_\theta^2 \Upsilon_{\omega,\theta} = \Upsilon_{\omega,\theta} \sigma_\theta^2,\tag{17}$$

where, for each $\theta \in \Theta$, and $\omega \in [-\pi, \pi]$, $\omega \neq 0$, $\Upsilon_{\omega,\theta}$ has kernel $\mathcal{K}_{\Upsilon_{\omega,\theta}}$ such that

$$\int_{-\pi}^{\pi} \int_{\mathbb{M}_d} \mathcal{K}_{\Upsilon_{\omega,\theta}}(\mathbf{x}, \mathbf{y}) \mathcal{K}_{\mathcal{W}_\omega}(\mathbf{y}, \mathbf{z}) d\nu(\mathbf{y}) d\omega = \delta(\mathbf{x} - \mathbf{z}), \quad \mathbf{x}, \mathbf{z} \in \mathbb{M}_d,\tag{18}$$

in the $L^2(\mathbb{M}_d, d\nu; \mathbb{C})$ sense, with $\delta(\mathbf{x} - \mathbf{y})$ denoting the Dirac Delta distribution. Thus, for every $\varrho, \psi \in L^2(\mathbb{M}_d, d\nu; \mathbb{C})$,

$$\int_{-\pi}^{\pi} \Upsilon_{\omega,\theta} \mathcal{W}_\omega(\varrho)(\psi) d\omega = \langle \varrho, \psi \rangle_{L^2(\mathbb{M}_d, d\nu; \mathbb{C})}.\tag{19}$$

Equation (19) means that $\int_{-\pi}^{\pi} \Upsilon_{\omega,\theta} \mathcal{W}_\omega d\omega$ defines the identity operator $\mathcal{I}_{L^2(\mathbb{M}_d, d\nu; \mathbb{C})}$ on $L^2(\mathbb{M}_d, d\nu; \mathbb{C})$, for each $\theta \in \Theta$.

Let us now consider the empirical contrast operator $\mathbf{U}_{T,\theta}$ given by, for each $\theta \in \Theta$,

$$\mathbf{U}_{T,\theta} = - \int_{-\pi}^{\pi} p_\omega^{(T)} \ln(\Upsilon_{\omega,\theta}) \mathcal{W}_\omega d\omega,\tag{20}$$

where, as before, $p_\omega^{(T)}$ denotes the periodogram operator computed from the fDFT introduced in equation (11), based on a functional sample of size T , $\tilde{X}_1(\cdot), \dots, \tilde{X}_T(\cdot)$. For each $\theta \in \Theta$, U_θ is the theoretical counterpart of $\mathbf{U}_{T,\theta}$, having kernel \mathcal{K}_{U_θ} given by, for $\mathbf{x}, \mathbf{y} \in \mathbb{M}_d$,

$$\begin{aligned} \mathcal{K}_{U_\theta}(\mathbf{x}, \mathbf{y}) = & - \sum_{n \geq 0} P_n^{(\alpha, \beta)}(\cos(d_{\mathbb{M}_d}(\mathbf{x}, \mathbf{y}))) \int_{-\pi}^{\pi} \frac{B_n^\eta(0) M_n(\omega)}{[4(\sin(\omega/2))^2]^{\alpha(n, \theta)/2}} \\ & \times \ln(\Upsilon(\omega, n, \theta)) |\omega|^{-\gamma} \widetilde{W}(n) d\omega, \end{aligned} \quad (21)$$

where, from (18)–(19), for each $n \in \mathbb{N}_0$, $\Upsilon(\omega, n, \theta)$ is such that

$$\int_{-\pi}^{\pi} \Upsilon(\omega, n, \theta) W(n, \omega, \gamma) d\omega = 1, \quad \forall \theta \in \Theta. \quad (22)$$

Hence, $U_\theta \in \mathcal{L}(L^2(\mathbb{M}_d, d\nu; \mathbb{C}))$ (see also Remark 7 in [37]). The eigenvalues of U_θ are then given by

$$U_\theta(n) = -\widetilde{W}(n) \int_{-\pi}^{\pi} \frac{B_n^\eta(0) M_n(\omega)}{[4(\sin(\omega/2))^2]^{\alpha(n, \theta)/2}} \ln(\Upsilon(\omega, n, \theta)) |\omega|^{-\gamma} d\omega, \quad n \geq 0. \quad (23)$$

The loss function $\|U_\theta - U_{\theta_0}\|_{\mathcal{L}(L^2(\mathbb{M}_d, d\nu; \mathbb{C}))}$ to be minimized is defined in the norm of the space $\mathcal{L}(L^2(\mathbb{M}_d, d\nu; \mathbb{C}))$ of bounded linear operators, providing a measure of the discrepancy between the minimum contrast operators U_θ and U_{θ_0} , respectively defined from the frequency varying candidate operator family $\Upsilon_{\omega, \theta}$, $\omega \in [-\pi, \pi]$, $\theta \in \Theta$, and the true parametric operator model $\Upsilon_{\omega, \theta_0}$, $\omega \in [-\pi, \pi]$. Specifically, in a theoretical framework, the following minimization problem is considered:

$$\begin{aligned} \min_{\theta \in \Theta} \|U_\theta - U_{\theta_0}\|_{\mathcal{L}(L^2(\mathbb{M}_d, d\nu; \mathbb{C}))} &:= \min_{\theta \in \Theta} [L(\theta_0, \theta)] \\ &= \min_{\theta \in \Theta} \left\| \int_{-\pi}^{\pi} \mathcal{F}_{\omega, \theta_0} \ln(\Upsilon_{\omega, \theta_0} \Upsilon_{\omega, \theta}^{-1}) \mathcal{W}_\omega d\omega \right\|_{\mathcal{L}(L^2(\mathbb{M}_d, d\nu; \mathbb{C}))} \\ &= \min_{\theta \in \Theta} \left\{ \sup_{n \geq 0} \left| \widetilde{W}(n) \int_{-\pi}^{\pi} \frac{f_{n, \theta}(\omega)}{|\omega|^{-\gamma}} \ln \left(\frac{\Upsilon(\omega, n, \theta_0)}{\Upsilon(\omega, n, \theta)} \right) d\omega \right| \right\}. \end{aligned} \quad (24)$$

The introduced loss function $L(\theta_0, \theta)$ in (24) defines an infinite-dimensional version of the contrast function based on Ibragimov contrast functional. From equations (15)–(24), applying Jensen's inequality and identity (22), for $\theta \in \Theta$,

and for each $n \geq 0$,

$$\begin{aligned} & -\widetilde{W}(n) \int_{-\pi}^{\pi} \frac{f_{n,\theta}(\omega)}{|\omega|^{-\gamma}} \ln \left(\frac{\Upsilon(\omega, n, \theta_0)}{\Upsilon(\omega, n, \theta)} \right) d\omega \\ & \leq \|\sigma_{\theta}^2\|_{\mathcal{L}(L^2(\mathbb{M}_d, d\nu; \mathbb{C}))} \ln \left(\int_{-\pi}^{\pi} \Upsilon(\omega, n, \theta) W(\omega, n, \gamma) d\omega \right) = 0. \end{aligned} \quad (25)$$

Thus, for every $n \geq 0$, and $\theta \in \Theta$,

$$L_n(\theta_0, \theta) = \widetilde{W}(n) \int_{-\pi}^{\pi} \frac{f_{n,\theta}(\omega)}{|\omega|^{-\gamma}} \ln \left(\frac{\Upsilon(\omega, n, \theta_0)}{\Upsilon(\omega, n, \theta)} \right) d\omega \geq 0.$$

Hence,

$$\begin{aligned} L(\theta_0, \theta) &= \sup_{n \geq 0} L_n(\theta_0, \theta) > 0, \quad \theta \neq \theta_0 \\ L(\theta_0, \theta) &= \sup_{n \geq 0} L_n(\theta_0, \theta) = 0 \Leftrightarrow \theta = \theta_0. \end{aligned} \quad (26)$$

From equation (26),

$$\begin{aligned} \theta_0 &= \arg \min_{\theta \in \Theta} \sup_{n \geq 0} L_n(\theta_0, \theta) \\ &= \arg \min_{\theta \in \Theta} \sup_{n \geq 0} U_{\theta}(n), \end{aligned} \quad (27)$$

where $U_{\theta}(n)$ has been introduced in equation (23) for $n \geq 0$.

We then consider the following estimator $\widehat{\theta}_T$ computed from the empirical contrast operator $\mathbf{U}_{T,\theta}$ in (20):

$$\widehat{\theta}_T = \arg \min_{\theta \in \Theta} \left\| - \int_{-\pi}^{\pi} p_{\omega}^{(T)} \ln(\Upsilon_{\omega,\theta}) \mathcal{W}_{\omega} d\omega \right\|_{\mathcal{L}(L^2(\mathbb{M}_d, d\nu; \mathbb{C}))} \quad (28)$$

(see also Section 5 in [37]).

The following result provides weak-consistency of the minimum contrast parameter estimator $\mathcal{A}_{\widehat{\theta}_T}$ of the log-memory operator.

Theorem 2 *Let $\{\widetilde{X}_t, t \in \mathbb{Z}\}$ be a Gaussian $L^2(\mathbb{M}_d, d\nu)$ -valued sequence satisfying (2)–(3), and **Conditions C0–C1**. Assume that the slowly varying functions at $\omega = 0$, $\{M_n(\omega), \omega \in [-\pi, \pi], n \in \mathbb{N}_0\}$, in equation (6), are such that, for any $\xi > 0$,*

$$\lim_{\omega \rightarrow 0} \left[\sup_{n \in \mathbb{N}_0} \left| \frac{M_n(\omega/\xi)}{M_n(\omega)} - 1 \right| \right] = 0. \quad (29)$$

The minimum contrast estimator (28), introduced in equations (13)–(27) with $\gamma > 1$, then satisfies

$$E \left\| \int_{-\pi}^{\pi} [p_{\omega}^{(T)} - \mathcal{F}_{\omega, \theta_0}] \mathcal{W}_{\omega, \theta} d\omega \right\|_{\mathcal{S}(\tilde{H})} \rightarrow 0, \quad T \rightarrow \infty, \quad (30)$$

where, for $(\omega, \theta) \in [-\pi, \pi] \setminus \{0\} \times \Theta$,

$$\mathcal{W}_{\omega, \theta} = \ln(\Upsilon_{\omega, \theta}) \mathcal{W}_{\omega}. \quad (31)$$

Remark 4 From Theorem 2, the following convergence in probability (\rightarrow_P) holds:

$$\hat{\theta}_T \rightarrow_P \theta_0, \quad T \rightarrow \infty.$$

Proof. The proof follows straightforward from Theorem 2 in [37]. In particular, the minimum contrast estimators

$$\left\{ \hat{\alpha}_T(n, \theta_0) = \alpha(n, \hat{\theta}_T), \quad n \in \mathbb{N}_0 \right\}$$

of the eigenvalues $\{\alpha(n, \theta_0), \quad n \in \mathbb{N}_0\}$ of the parametric long-memory operator \mathcal{A}_{θ_0} are weak-consistent.

4 SRD–LRD estimation in the spectral domain

This section addresses the case where in **Condition C1**, $l_{\alpha}(\theta) = 0$, and $\alpha(n, \theta) = 0$, for $n \in \mathcal{D}_{\text{SRD}} \subset \mathbb{N}_0$. Particularly, the projected manifold process displays SRD at discrete Jacobi frequencies $n \in \mathcal{D}_{\text{SRD}}$. Without loss of generality we consider $\mathcal{D}_{\text{SRD}} = \{0, \dots, n_0\}$, for certain $n_0 \in \mathbb{N}_0$. In Section 5.2, we will illustrate the complementary case. The projection of the manifold process $\{\tilde{X}_t(\cdot), \quad t \in \mathbb{T}\}$ into the subspace generated by $\{P_n^{(\alpha, \beta)}, \quad n \leq n_0\}$ leads to the definition of a SRD process admitting the following expression:

$$\tilde{X}_t^{(n_0)}(\mathbf{x}) = \sum_{n=0}^{n_0} V_n(t) P_n^{(\alpha, \beta)}(\cos(d_{\mathbb{M}_d}(\mathbf{x}, \mathbf{U}))), \quad \mathbf{x} \in \mathbb{M}_d, \quad t \in \mathbb{Z}. \quad (32)$$

From equation (32), for $\omega \in [-\pi, \pi]$, the projection

$$\tilde{X}_{\omega}^{(T, n_0)}(\mathbf{x}) = \frac{1}{\sqrt{2\pi T}} \sum_{n=0}^{n_0} \sum_{t=1}^T V_n(t) \exp(-i\omega t) P_n^{(\alpha, \beta)}(\cos(d_{\mathbb{M}_d}(\mathbf{x}, \mathbf{U}))) \quad (33)$$

of the fDFT into the subspace generated by $\{P_n^{(\alpha,\beta)}, n \leq n_0\}$ is involved in the definition of the finite-dimensional periodogram $p_\omega^{(T,n_0)} = \widetilde{X}_\omega^{(T,n_0)} \otimes \overline{\widetilde{X}_\omega^{(T,n_0)}}$, providing the empirical second-order structure in the spectral domain of the projected manifold process $\widetilde{X}_t^{(n_0)}$ displaying SRD.

The following nonparametric estimator, based on the weighted periodogram operator, is then computed (see [31]): For $\omega \in [-\pi, \pi]$,

$$\widehat{f}_\omega^{(T,n_0)}(\mathbf{x}, \mathbf{y}) = \left[\frac{2\pi}{T} \right] \sum_{t \in [1, T-1]} W^{(T)} \left(\omega - \frac{2\pi t}{T} \right) p_{2\pi t/T}^{(T,n_0)}(\mathbf{x}, \mathbf{y}), \quad \forall \mathbf{x}, \mathbf{y} \in \mathbb{M}_d, \quad (34)$$

where the weight function $W^{(T)}$ satisfies

$$W^{(T)}(x) = \sum_{j \in \mathbb{Z}} \frac{1}{B_T} W \left(\frac{x + 2\pi j}{B_T} \right), \quad (35)$$

with B_T being the positive bandwidth parameter, and W being a real function defined on \mathbb{R} such that

- (1) W is positive, even, and bounded in variation
- (2) $W(x) = 0$, if $|x| \geq 1$;
- (3) $\int_{\mathbb{R}} |W(x)|^2 dx < \infty$
- (4) $\int_{\mathbb{R}} W(x) dx = 1$.

In the approximation of the projected spectral density operator family at the remaining Jacobi frequencies, under **Condition C1**, the minimum contrast parameter estimator $\widehat{\alpha}_T(n, \theta_0) = \alpha(n, \widehat{\theta}_T)$ is computed as before, for $n > n_0$. Thus, for every Jacobi frequency $n \in \mathbb{N}_0$, the following estimator of the kernel of the spectral density operator is considered: For $\omega \in [-\pi, \pi] \setminus \{0\}$, and $\mathbf{x}, \mathbf{y} \in \mathbb{M}_d$,

$$\begin{aligned} \widehat{f}_\omega^{(T)}(\mathbf{x}, \mathbf{y}) &= \widehat{f}_\omega^{(T,n_0)}(\mathbf{x}, \mathbf{y}) + \widehat{f}_\omega^{(T,(n_0+1,\infty))}(\mathbf{x}, \mathbf{y}, \widehat{\theta}_T) \\ &= \left[\frac{2\pi}{T} \right] \sum_{t \in [1, T-1]} W^{(T)} \left(\omega - \frac{2\pi t}{T} \right) p_{2\pi t/T}^{(T,n_0)}(\mathbf{x}, \mathbf{y}) \\ &\quad + \sum_{n=n_0+1}^{\infty} \frac{B_n^\eta(0) M_n(\omega)}{[4(\sin(\omega/2))^2]^{\alpha(n, \widehat{\theta}_T)/2}} P_n^{(\alpha,\beta)}(\cos(d_{\mathbb{M}_d}(\mathbf{x}, \mathbf{y}))), \end{aligned} \quad (36)$$

where, from (33), the empirical kernel of the projected periodogram operator $p_\omega^{(T,n_0)}$ is expressed in terms of the tensorial product of the Jacobi polynomials up to order n_0 , and $\{M_n, n \in \mathbb{N}_0\}$ satisfies as before **Condition C1**.

5 Simulation study

LRD functional time series models defined by multifractional integration of SPHMA(p) processes are numerically analyzed in Section 5.1, considering the case where the projected spherical process displays LRD at every Legendre frequency, and the sequence of eigenvalues of the bounded long-memory operator is increasing. Hence, spherical small and large scale behaviors persist in time, with stronger persistence at small scale. In Section 5.2, multifractionally integrated SPHARMA(p,q) processes are generated considering the parameter values $p = 1$ and $q = 1$. Under this scenario, we analyze the case where the spherical projected process displays LRD at low discrete Legendre frequencies, while SRD is observed at high frequencies. Spherical large scale behavior then persists in time while higher variability is observed at spherical small scales.

5.1 Multifractionally integrated SPHAR(p) processes

Beyond the Hilbert–Schmidt operator assumption on the autoregressive operators involved in the definition of SPHAR(p) processes introduced in [12], a multifractionally integrated SPHAR(3) process is generated here with autoregressive isotropic operators in the space $\mathcal{L}(L^2(\mathbb{S}_2, d\nu))$. Note that the trace property of the autocovariance operator of the Gaussian strong-white noise innovation process ensures the trace property of the autocovariance operator of $\{\tilde{X}_t, t \in \mathbb{Z}\}$, when the autoregressive operators are assumed to be bounded operators (see, e.g., [9]). Thus, **Condition C0** holds (see equation (3.18) in [37]). In this section, in the Gaussian case, under **Assumption I** in Theorem 2 in [37], the weak consistency of the minimum contrast parameter estimator of the long-memory operator is illustrated (see also [12] for the consistent least-squares estimation of the functional autoregressive parameters of SPHAR processes).

Our LRD functional time series process $\{\tilde{X}_t, t \in \mathbb{Z}\}$ satisfies the state equation

$$\begin{aligned} (\mathcal{I}_{L^2(\mathbb{M}_d, d\nu)} - B)^{\mathcal{A}_\theta/2} \tilde{X}_t(\mathbf{x}) &= (\Phi_3(B)\tilde{X}_t)(\mathbf{x}) + \varepsilon_t(\mathbf{x}) \\ &= (\Phi_1\tilde{X}_{t-1})(\mathbf{x}) + (\Phi_2\tilde{X}_{t-2})(\mathbf{x}) + (\Phi_3\tilde{X}_{t-3})(\mathbf{x}) + \varepsilon_t(\mathbf{x}), \end{aligned} \tag{37}$$

for $(\mathbf{x}, t) \in \mathbb{M}_d \times \mathbb{Z}$, where B denotes the difference operator (see Section 3.3. in [37]), and $\mathcal{I}_{L^2(\mathbb{M}_d, d\nu)}$ is the identity operator over the space $L^2(\mathbb{M}_d, d\nu)$. Here, $\{\varepsilon_t(\mathbf{x}), \mathbf{x} \in \mathbb{M}_d, t \in \mathbb{Z}\}$ represents $L^2(\mathbb{M}_d, d\nu)$ -valued Gaussian strong-white noise (see [9]). Equation (37) holds in the mean-square sense, and in

the space $L^2_{L^2(\mathbb{M}_d, d\nu)}(\Omega)$. The autoregressive operators Φ_i , $i = 1, 2, 3$, defining the autoregression $\Phi_3(z) = \sum_{i=1}^3 \Phi_i z^i$ have respective kernels ϕ_i , $i = 1, 2, 3$, invariant under all isometries of \mathbb{M}_d . In the generations we consider the special case of $d = 2$ and $\mathbb{M}_2 = \mathbb{S}_2$. The following diagonal spectral representation then holds

$$\phi_i(\mathbf{x}, \mathbf{y}) = \sum_{n=0}^{\infty} \phi_n^{(i)} \frac{2n+1}{4\pi} P_n(\langle \mathbf{x}, \mathbf{y} \rangle), \quad \mathbf{x}, \mathbf{y} \in \mathbb{S}_2, \quad i = 1, 2, 3, \quad (38)$$

in the space $L^2(\mathbb{S}_2, d\nu)$, for kernels ϕ_i , $i = 1, 2, 3$, involving the spherical harmonics $\{Y_{m,l}, m = -l, \dots, l, l \geq 0\}$ by the identity

$$\sum_{m=-l}^l Y_{m,l}(\mathbf{x}) Y_{m,l}(\mathbf{y}) = \frac{(2l+1)}{4\pi} P_l(\langle \mathbf{x}, \mathbf{y} \rangle), \quad \mathbf{x}, \mathbf{y} \in \mathbb{S}_2, \quad l \geq 0, \quad (39)$$

in terms of the Legendre polynomial orthogonal basis $\{P_l, l \geq 0\}$. In the subsequent estimation results, we consider a truncated version of model (37), with $\phi_n^{(1)} = 0.6(n/(n+1))$, $\phi_n^{(2)} = 0.2(n/(n+1))$, and $\phi_n^{(3)} = -0.1(n/(n+1))$, $n = 1, \dots, 30$ (see Figures 1–2). Figure 1 displays the temporal $\{V_n\}$ coefficients of spatiotemporal random field X at Legendre frequencies $n = 1, 4, 7, 10, 13, 16, 19, 22, 25, 28$, for $T = 100$. Although the posterior numerical analysis is based on functional samples \tilde{X}_t , $t = 1, \dots, T$, of sizes $T = 100, \dots, 1000$ (see Figures 9 and 10). Figure 2 also shows the corresponding temporal random coefficients of the $L^2(\mathbb{S}_2, d\nu)$ -valued Gaussian strong-white noise process. Figure 3 finally provides the functional spherical values of the generated Gaussian multifractionally integrated SPHAR(3) process, whose $L^2(\mathbb{S}_2, d\nu)$ -valued Gaussian strong-white noise innovation process has variance $\sigma_\varepsilon^2 = \sum_{n \in \mathbb{N}_0} \sigma_n^2$, with $\sigma_n^2 = (0.01(n/n+1))^{-3/2}$, $n \in \mathbb{N}$. It can be observed in this figure that both, spherical small and large scale behaviors persist in time, with stronger persistence of spherical small scale than large scale patterns. Particularly, one can observe some variability in the almost null values (blue color) over the peripheral ring (see Figures 3).

The parameterized eigenvalues $\{\alpha(n, \theta), n \in \mathbb{N}_0, \theta \in \Theta\}$ of the long-memory operator \mathcal{A}_θ are displayed for $\theta = \theta_0$, the true parameter value, at the left-hand side of Figure 4. The set of 50 candidates $\{\alpha(n, \theta_i), n \in \mathbb{N}_0, i = 1, \dots, 50\}$ (50 systems of parameterized eigenvalues) considered in the implementation of the minimum contrast estimation procedure are showed at the right-hand side of Figure 4. They obey the following equations

$$\begin{aligned} \alpha(n, \theta_0) &= \frac{1}{10} \left[\frac{\exp(-(\theta_{0,2} + \theta_{0,3}n))}{\theta_{0,1}} + 1 \right], \quad \theta_0 = (\theta_{0,1}, \theta_{0,2}, \theta_{0,3}) = (-9, 1, 1) \\ \alpha(n, \theta_i) &= \frac{1}{10} \left[\frac{\exp(-(\theta_{i,2} + \theta_{i,3}n))}{\theta_{i,1}} + 1 \right], \quad i = 1, \dots, 50 \end{aligned}$$

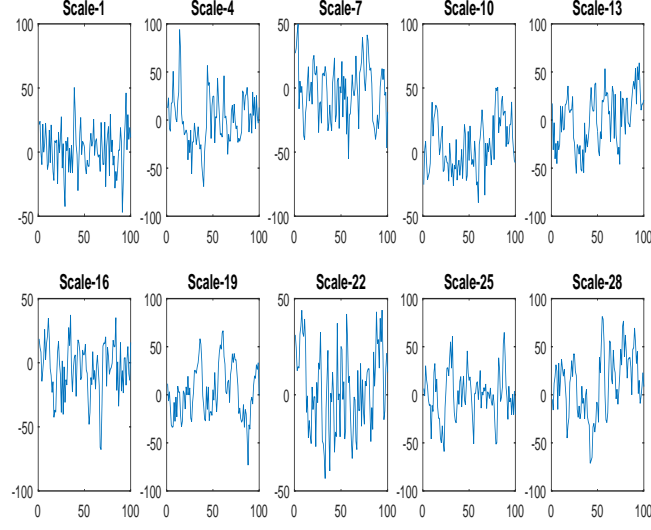


Figure 1: V_n random coefficients of the Gaussian multifractionally integrated SPHAR(3) process \tilde{X} (100 temporal nodes) at Legendre frequencies $n = 1, 4, 7, 10, 13, 16, 19, 22, 25, 28$.

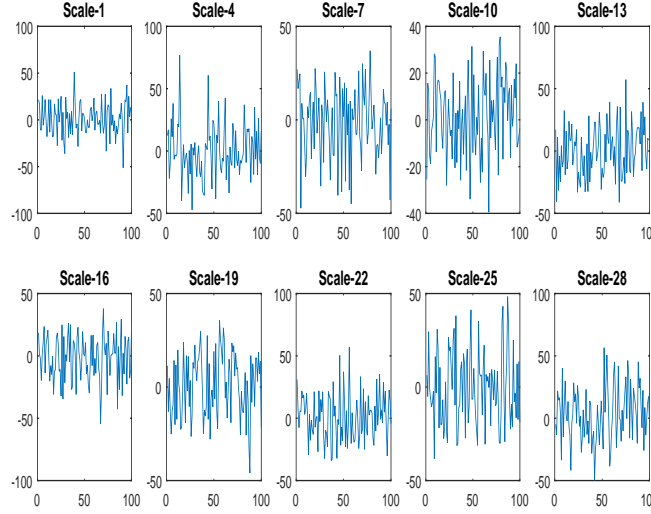


Figure 2: Random coefficients of the $L^2(\mathbb{S}_2, d\nu)$ -valued Gaussian strong-white noise innovation process ε (100 temporal nodes) at Legendre frequencies $n = 1, 4, 7, 10, 13, 16, 19, 22, 25, 28$.

$$\theta_i = (\theta_{i,1}, \theta_{i,2}, \theta_{i,3}) = \left(-70, 1 + \frac{i}{50}, 1 + \frac{i+1}{50} \right), \quad i = 1, \dots, 50. \quad (40)$$

For $n = 1, \dots, 30$, and $i = 1, \dots, 100$, the sequences $[4(\sin(\omega_i/2))^2]^{-\alpha(n,\theta)/4}$

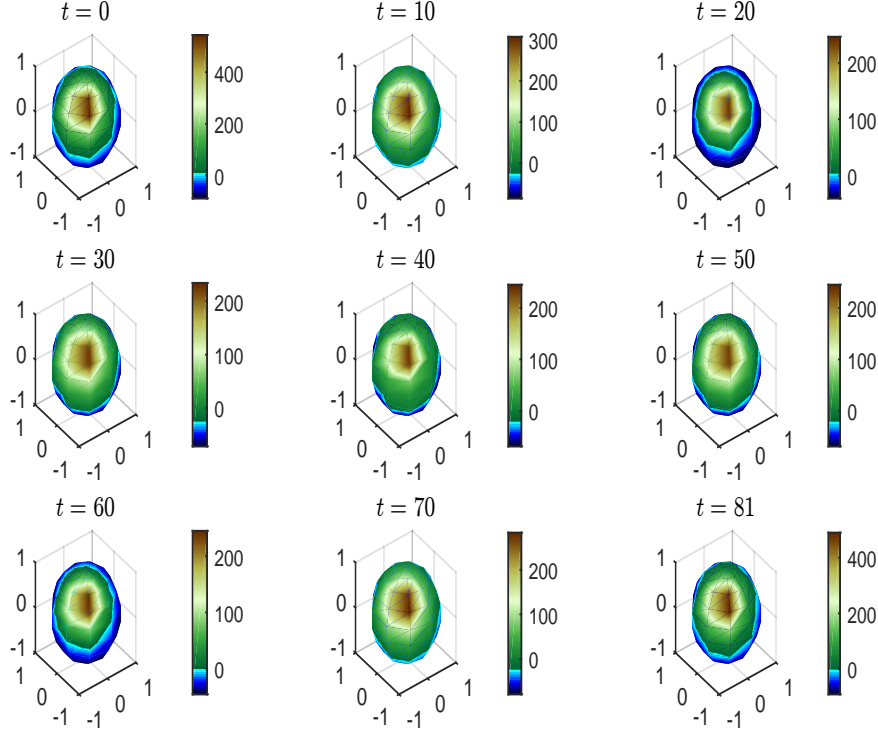


Figure 3: Generations of Gaussian multifractionally integrated SPHAR(3) process \tilde{X} at times $t = 0, 10, 20, 30, 40, 50, 60, 70, 81$.

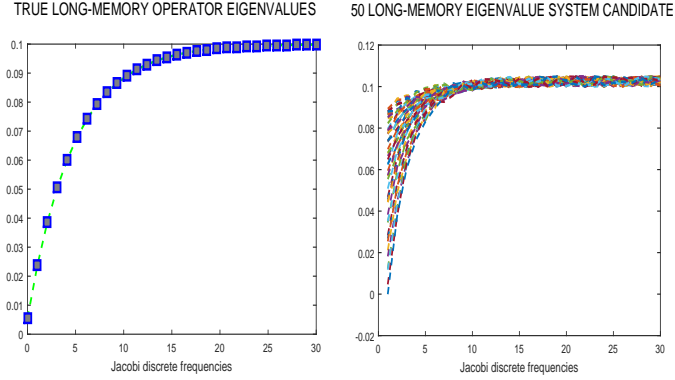


Figure 4: *Non-compact self-adjoint bounded positive long-memory operator*. The theoretical first 30 eigenvalues $\alpha(n, \theta_0)$, $n = 0, \dots, 30$ (left-hand side). The first 30 eigenvalues $\alpha(n, \theta_i)$, $n = 0, \dots, 30$, of the long-memory operator candidate \mathcal{A}_{θ_i} , $i = 1, \dots, 50$ (right-hand side)

(left-hand side), $|M_n(\omega_i)|^{1/2}$ (center) and $[4(\sin(\omega_i/2))^2]^{-\alpha(n, \theta)/4} |M_n(\omega_i)|^{1/2}$ (right-hand side) are displayed in Figure 5. Figure 6 provides the projected

spectral density operator kernel over 30×30 discrete Legendre frequencies at temporal Fourier frequencies $\omega = -\pi + 0.0628(10)i$, $i = 1, 3, 7, 10$ in the interval $[-\pi, \pi]$. Its empirical counterpart is given in Figure 7 where the projected fDFT, and tapered periodogram operator kernel of the generated data at frequency zero are displayed. The last one over a grid of 30×30 Legendre frequencies. After normalization by integration over the interval $[-\pi, \pi]$, the projected empirical contrast operator $\mathbf{U}_{T,\theta}$ in equation (20) is computed, for the 30 Legendre frequencies involved in the truncation, and the 50 candidate parametric models considered. Figure 8 displays the empirical probabilities

$$\hat{\mathcal{P}} \left(\|f_{n,\theta_0}(\omega) - f_{n,\hat{\theta}_T}(\omega)\|_{L^2([-\pi,\pi])} > \varepsilon_i \right),$$

for $n = 1, \dots, 30$, and $\varepsilon_i = i(0.012) \in (0, 0.6)$, $i = 1, \dots, 50$, based on 100 repetitions, when the estimator $f_{n,\hat{\theta}_T}(\omega)$ is computed by minimizing the norm of the empirical contrast operator $\mathbf{U}_{T,\theta}$ in the space of bounded linear operators $\mathcal{L}(L^2(\mathbb{S}_2, d\nu; \mathbb{C}))$, and in the space of Hilbert–Schmidt operators $\mathcal{S}(L^2(\mathbb{S}_2, d\nu; \mathbb{C}))$. We display in both cases the histograms of the empirical mean quadratic errors (EMQEs) based on the functional samples of sizes $T = 100$, and $T = 1000$ (see Figures 9 and 10).

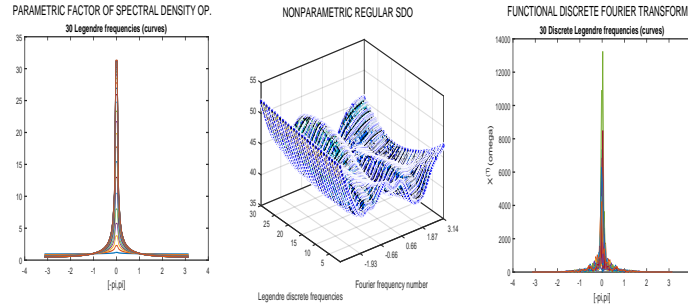


Figure 5: Parametric part of the square root of the projected spectral density operator at Legendre frequencies $n = 1, \dots, 30$ (left-hand side). Nonparametric regular factor of the square root of the projected spectral density operator (SDO) at Legendre frequencies $n = 1, \dots, 30$ (center). The square root of the spectral density operator at Legendre frequencies $n = 1, \dots, 30$ (right-hand side)

5.2 Multifractionally integrated SPHARMA(p,q) processes displaying SRD and LRD at different spherical scales

A multifractionally integrated SPHARMA(1,1) model is generated by considering a bounded long-memory operator with null eigenvalues at discrete

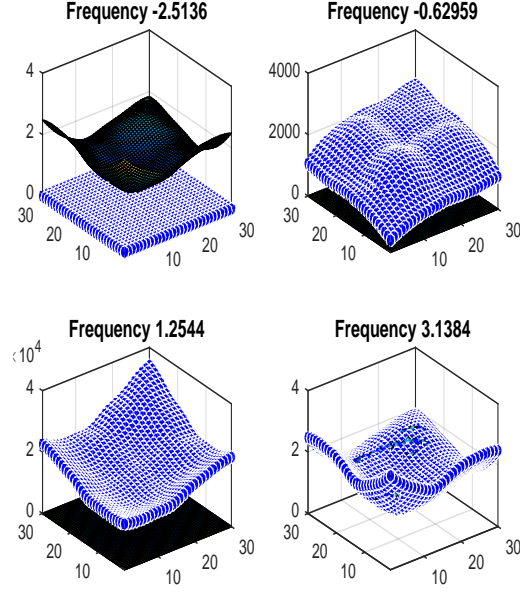


Figure 6: Spectral Density Operator (SDO) kernel of $\mathcal{F}_{\omega, \theta_0}$ over regular grid of 30×30 discrete Legendre frequencies, for temporal Fourier frequencies $\omega = -\pi + 0.0628(10)i$, $i = 1, 3, 7, 10$

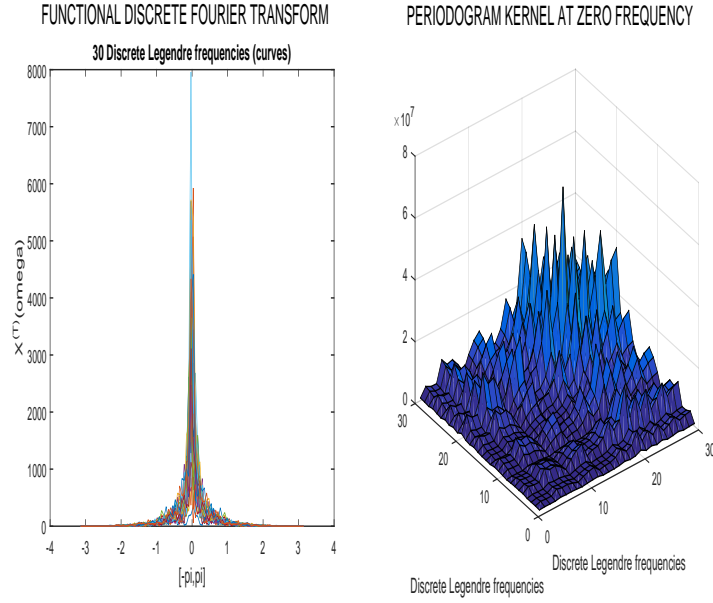


Figure 7: fDFT of the data (30 spectral curves) corresponding to 30 Legendre frequencies (left-hand side). Tapered periodogram kernel at zero temporal Fourier frequency over a 30×30 grid of discrete Legendre frequencies (right-hand side)

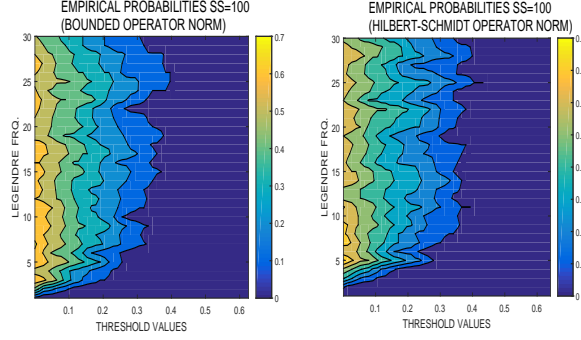


Figure 8: The empirical probabilities $\hat{\mathcal{P}}\left(\|f_{n,\theta_0}(\omega) - f_{n,\hat{\theta}_T}(\omega)\|_{L^2([-\pi,\pi])} > \varepsilon_i\right)$, for $n = 1, \dots, 30$, and $\varepsilon_i = i(0.012) \in (0, 0.6)$, $i = 1, \dots, 50$, based on 100 repetitions, when the $\mathcal{L}(L^2(\mathbb{M}_d, d\nu; \mathbb{C}))$ (left-hand side) and $\mathcal{S}(L^2(\mathbb{M}_d, d\nu; \mathbb{C}))$ (right-hand side) norms of the empirical contrast operator are minimized

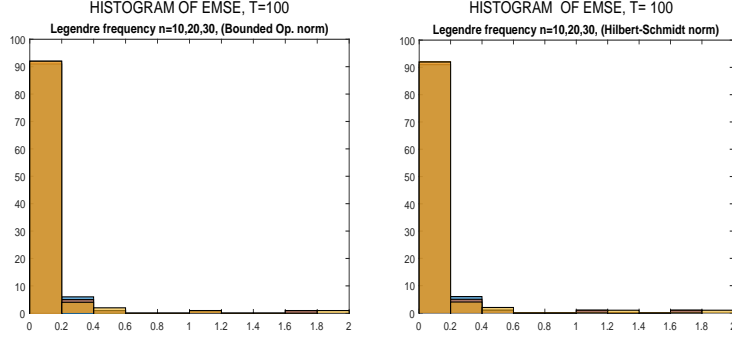


Figure 9: Histograms of the Empirical Mean Square Errors (EMSE) at Legendre frequencies $n = 10, 20, 30$, based on a functional sample of size $T = 100$, for the minimum contrast parameter estimator, computed by minimizing the norm of the empirical contrast operator in the space $\mathcal{L}(L^2(\mathbb{M}_d, d\nu; \mathbb{C}))$ (left-hand side), and in the space $\mathcal{S}(L^2(\mathbb{M}_d, d\nu; \mathbb{C}))$ (right-hand side)

Legendre frequencies $n = 16, \dots, 30$. Particularly, our LRD functional time series process $\{\tilde{X}_t, t \in \mathbb{Z}\}$ satisfies the state equation

$$\begin{aligned} (\mathcal{I}_{L^2(\mathbb{S}_2, d\nu)} - B)^{\mathcal{A}_{\theta}/2} \tilde{X}_t(\mathbf{x}) &= (\Phi_1(B) \tilde{X}_t)(\mathbf{x}) + (\Psi_1(B) \varepsilon_t)(\mathbf{x}) \\ &= (\Phi_1 \tilde{X}_{t-1})(\mathbf{x}) + \varepsilon_t(\mathbf{x}) + (\Psi_1 \varepsilon_{t-1})(\mathbf{x}), \end{aligned} \tag{41}$$

for $(\mathbf{x}, t) \in \mathbb{S}_2 \times \mathbb{Z}$, where B denotes the difference operator (see Section 3.3. in [37]), and $\mathcal{I}_{L^2(\mathbb{S}_2, d\nu)}$ is the identity operator on the space $L^2(\mathbb{S}_2, d\nu)$. As before, $\{\varepsilon_t(\mathbf{x}), \mathbf{x} \in \mathbb{S}_2, t \in \mathbb{Z}\}$ represents Gaussian strong-white noise evaluated in the space $L^2(\mathbb{S}_2, d\nu)$. Equation (41) holds in the mean-square sense, and in the space $L^2_{L^2(\mathbb{S}_2, d\nu)}(\Omega)$ (see [9]). The invariant kernels ϕ_1 and ψ_1 of the autoregressive Φ_1 and the moving average Ψ_1 operators admit the following

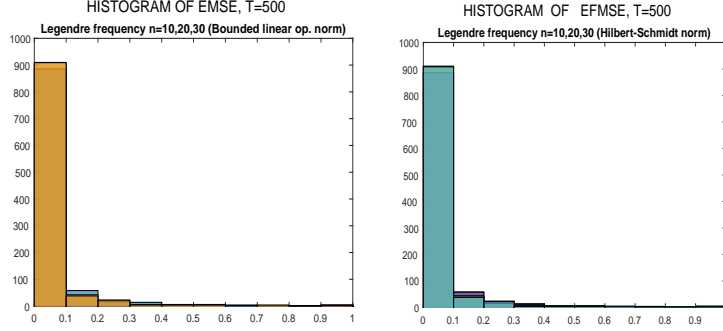


Figure 10: Histograms of the Empirical Mean Square Errors (EMSE) at Legendre frequencies $n = 10, 20, 30$, based on functional sample of size $T = 1000$, and minimization of the empirical minimum contrast operator in $\mathcal{L}(L^2(\mathbb{M}_d, d\nu; \mathbb{C}))$ norm (left-hand side), and in $\mathcal{S}(L^2(\mathbb{M}_d, d\nu; \mathbb{C}))$ norm (right-hand side)

diagonal spectral representations in terms of the Legendre polynomials:

$$\begin{aligned}\phi_1(\mathbf{x}, \mathbf{y}) &= \sum_{n=0}^{\infty} \phi_n^{(1)} \frac{2n+1}{4\pi} P_n(\langle \mathbf{x}, \mathbf{y} \rangle), \quad (\mathbf{x}, \mathbf{y}) \in \mathbb{S}_2 \\ \psi_1(\mathbf{x}, \mathbf{y}) &= \sum_{n=0}^{\infty} \psi_n^{(1)} \frac{2n+1}{4\pi} P_n(\langle \mathbf{x}, \mathbf{y} \rangle), \quad (\mathbf{x}, \mathbf{y}) \in \mathbb{S}_2.\end{aligned}\quad (42)$$

As before, a truncated version of model (41) is simulated, and the numerical results are displayed with reference to the Legendre frequencies $n = 1, \dots, 30$. Specifically, Figures 11–13 show generations for the particular case of $\phi_n^{(1)} = [0.7(n+1/n)]^{-3/2}$, and $\psi_n^{(1)} = [0.4(n+1/n)]^{-3/2}$, $n = 1, \dots, 30$. The $\{V_n\}$ coefficients are given in Figure 11, for discrete Legendre frequencies $n = 1, 2, 3, 4, 5, 6, 7, 8, 9, 10$, where still some structure is displayed, since for the remaining Legendre frequencies analyzed $n = 11, \dots, 30$, the behavior of these coefficients is very close to the one displayed by the Gaussian innovation strong white noise. Note that, here, we have adopted the setting of trace invariant autoregressive operators (see, e.g., [10] for the Hilbert–Schmidt operator case). As before, functional samples of size $T = 100, \dots, 1000$, are analyzed. Figure 12 provides the temporal random coefficients of the $L^2(\mathbb{S}_2, d\nu)$ –valued Gaussian strong–white noise at the same Legendre frequencies. Figure 13 finally displays the functional spherical values of the generated Gaussian multifractionally integrated SPHARMA(1,1) process, whose $L^2(\mathbb{S}_2, d\nu)$ –valued Gaussian strong–white noise innovations have variance $\sigma_\varepsilon^2 = \sum_{n \in \mathbb{N}_0} \sigma_n^2$, with $\sigma_n^2 = (0.015(n/n+1))^{-3/2}$, $n = 1, \dots, 30$. As announced, it can be observed a stronger persistence of the spherical large scale behavior with almost null values at every time at the peripheral ring, while some

fluctuations of the magnitude of the values displayed close to the origin are observed at short time periods (e.g., green-yellow colors run through the interval $(4, 15)$, from time $t = 0$ to time $t = 10$ in Figure 13).

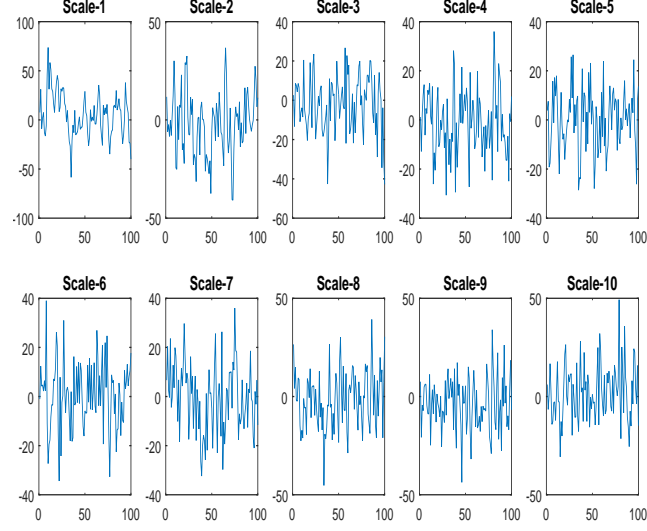


Figure 11: V_n random coefficients of the generated Gaussian multifractionally integrated SPHARMA(1,1) process (100 temporal nodes) at Legendre frequencies $n = 1, 2, 3, 4, 5, 6, 7, 8, 9, 10$.

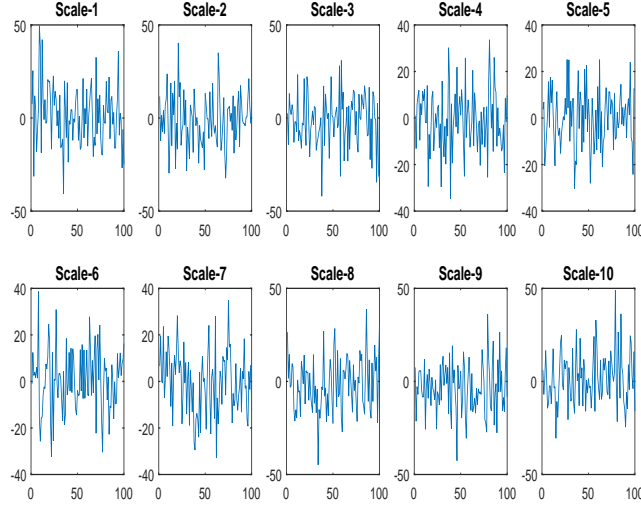


Figure 12: Random coefficients of the $L^2(\mathbb{S}_2, d\nu)$ -valued Gaussian strong-white noise innovation process ε (100 temporal nodes) at Legendre frequencies $n = 1, 2, 3, 4, 5, 6, 7, 8, 9, 10$.

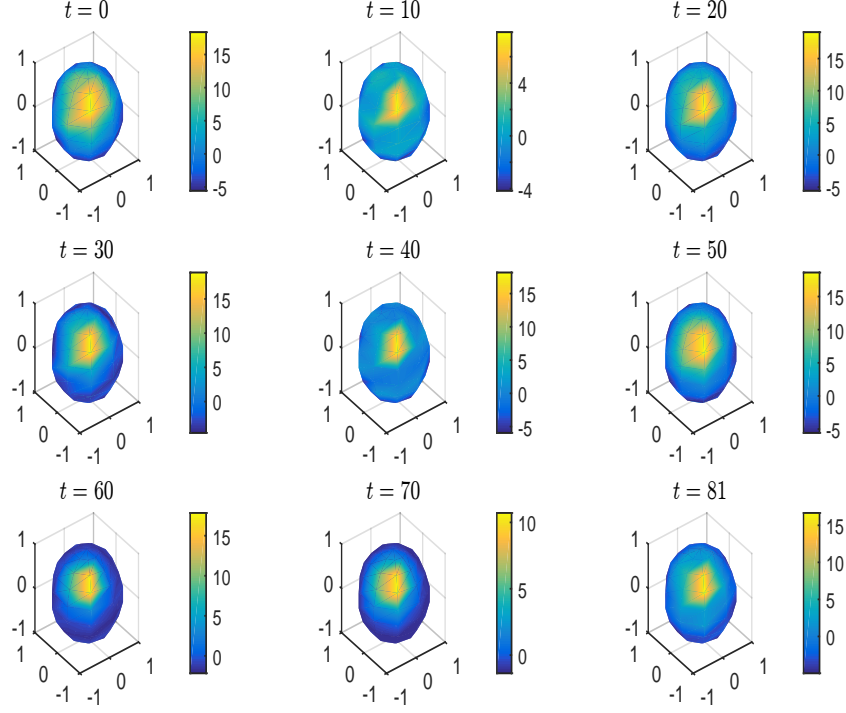


Figure 13: The generated Gaussian multifractionally integrated SPHARMA(1,1) for times $t = 0, 10, 20, 30, 40, 50, 60, 70, 81$.

The parameterized eigenvalues $\{\alpha(n, \theta), n \in \mathbb{N}_0, \theta \in \Theta\}$ of the long-memory operator \mathcal{A}_θ are displayed for $\theta = \theta_0$, the true parameter value, at the left-hand side of Figure 14. The set of 50 candidates $\{\alpha(n, \theta_i), n \in \mathbb{N}_0, i = 1, \dots, 50\}$ (50 systems of parameterized eigenvalues of the long-memory operator) considered in the implementation of the minimum contrast estimation procedure for $n = 1, \dots, 15$, are showed at the right-hand side of Figure 14. These families of parametric eigenvalues are obtained by sampling a scaled beta distribution with parameters 2 and $\frac{5i}{i+1}$, $i = 1, \dots, 50$.

In this example, the projected spherical process displays LRD for $n = 1, \dots, 15$, while SRD is observed at Legendre frequencies $n = 16, \dots, 30$. Thus, the opposite case to the one introduced in Section 4 is analyzed in this section. The modulus of the projected fDFT at Legendre frequencies $n = 1, \dots, 15$, where LRD is displayed, is showed in Figure 15. Figure 16 provides the modulus of the projected fDFT at Legendre frequencies $n = 16, \dots, 30$, where SRD is displayed. Figure 17 displays its nonparametric kernel estimate at such Legendre frequencies, based on the Gaussian

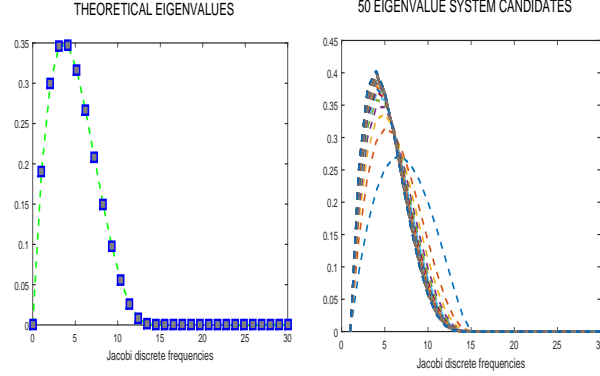


Figure 14: Eigenvalues of \mathcal{A}_{θ_0} for the case of SRD–LRD mixed models (left–hand side), and the eigenvalues of the 50 candidates \mathcal{A}_{θ_i} , $i = 1, \dots, 50$, considered (right–hand side).

kernel, and bandwidth parameter $B_{1000} = 0.65$, from the truncated version at $n = 30$ of the weighted periodogram operator estimator $\widehat{f}_{\omega}^{(T, (n_0+1, \infty))}$. This figure also provides the associated EMQEs for $T = 100$. Note that the magnitude order of these EMQEs is upper bounded by $2(10)^{-7}$ for $T = 1000$ (see, e.g., [31] where the asymptotic properties of the weighted periodogram operator estimator are derived). Let now $\widehat{f}_{\omega}^{(T, (n_0))}(\cdot, \widehat{\theta}_T)$ be the minimum contrast parametric estimator, with, here, $n_0 = 15$, providing the dimension of the space where LRD is displayed by the projected process. As before this estimator is obtained by minimizing over the 50 parametric models defining the candidates the $\mathcal{L}(L^2(\mathbb{S}_2, d\nu; \mathbb{C}))$ operator norm of the empirical contrast operator $\mathbf{U}_{T, \theta}$ in equation (20). Figure 18 displays the empirical probabilities

$$\widehat{\mathcal{P}} \left(\|f_n(\omega) - \widehat{f}_n^{(T, (n_0))}(\omega, \widehat{\theta}_T)\|_{L^2([- \pi, \pi])} > \varepsilon_i \right),$$

for $n = 1, \dots, 15$, and $\varepsilon_i = i(0.016) \in (0, 0.8)$, $i = 1, \dots, 50$, based on 100 repetitions. The histograms of the empirical mean quadratic errors of the mixed estimation $\widehat{f}_{\omega}^{(T)} = \widehat{f}_{\omega, (n_0)}^{(T)} + \widehat{f}_{\omega, (n_0+1, \infty)}^{(T)}$, based on respective functional samples of sizes $T = 100$, and $T = 1000$, and 100 repetitions, are also displayed in Figure 19. From the computed EMQEs for $T = 1000$, it can be observed a slightly better performance for large sample sizes, in the case of the mixed estimator $\widehat{f}_{\omega}^{(T)} = \widehat{f}_{\omega, (n_0)}^{(T)} + \widehat{f}_{\omega, (n_0+1, \infty)}^{(T)}$, due to the higher singularity of the model analyzed in Section 5.1, regarding the strongest LRD range, and the weaker boundedness assumption on the functional parameters involved in the autoregression.

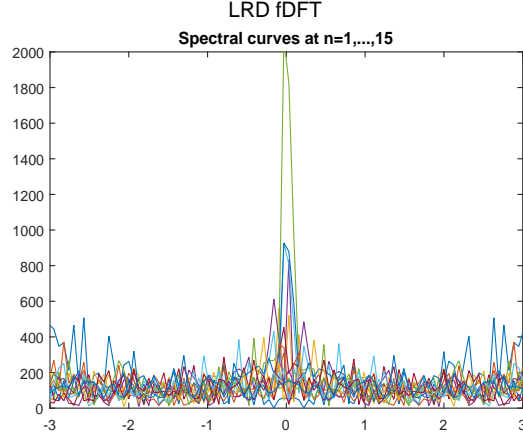


Figure 15: Modulus of the projected LRD fDFT for discrete Legendre frequencies $n = 1, \dots, 15$.

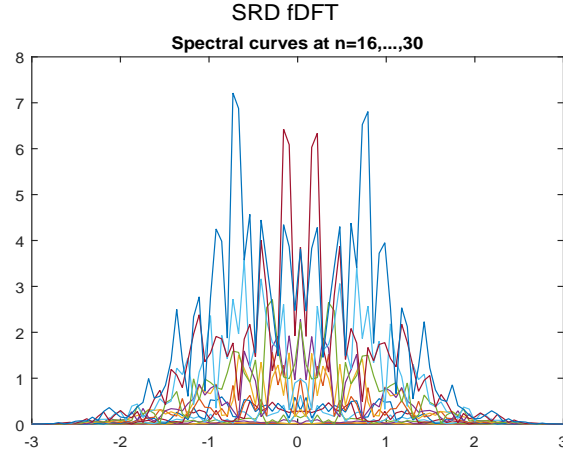


Figure 16: Modulus of the projected SRD fDFT for discrete Legendre frequencies $n = 16, \dots, 30$.

6 Final comments

A new family of models is presented in the LRD functional time series framework introduced in [37], considering the separable Hilbert space of square integrable functions on a connected and compact two-point homogeneous space. It is well-known the interest of these models, for example, in the field of Cosmic Microwave Background (CMB) evolution modeling and data analysis (see [2]; [5]; [19]; [14]; [15]; [25], among others). These models also arouse great interest in climatic change analysis from meteorological data,

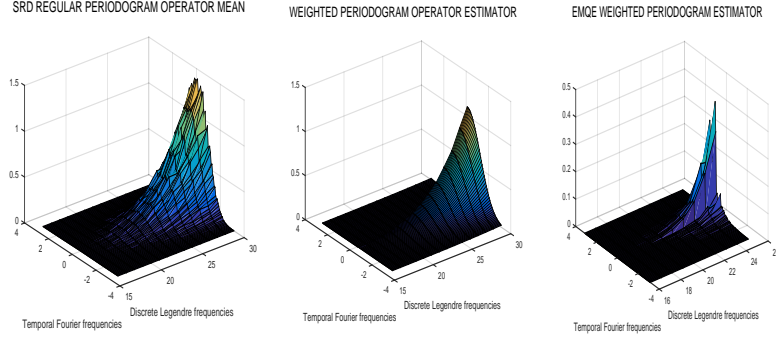


Figure 17: SRD projected square root of the spectral density operator $n = 16, \dots, 30$ (left-hand side). Its weighted periodogram estimator $n = 16, \dots, 30$ (center). Empirical mean square errors associated with the kernel estimator $\hat{f}_\omega^{(T, (n_0+1, \infty))}(\mathbf{x}, \mathbf{y})$ at Legendre frequencies $n = 16, \dots, 30$ (right-hand side)

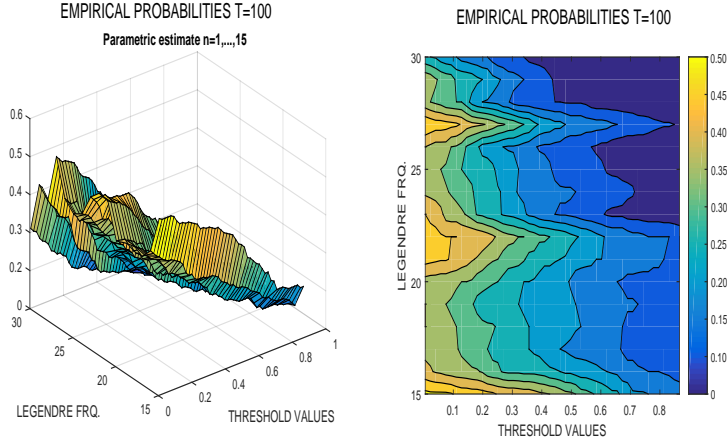


Figure 18: The empirical probabilities $\hat{\mathcal{P}}\left(\left\|f_n(\omega) - \hat{f}_\omega^{T, (n_0)}\right\|_{L^2([- \pi, \pi])} > \varepsilon_i\right)$, for $n = 1, \dots, 15$, and $\varepsilon_i = i(0.016) \in (0, 0.8)$, $i = 1, \dots, 50$, based on 100 repetitions, when the $\mathcal{L}(L^2(\mathbb{M}_d, d\nu; \mathbb{C}))$ norm of the empirical contrast operator is minimized (surface values are given at the left-hand and contour plot at the right-hand side).

regarding its effects on various atmospheric constituents and downward solar radiation flux (see, e.g., [1], where multivariate spherical random field models are applied in a Bayesian framework to a bivariate spatial data set from two 2019 NCEP/NCAR Flux Reanalyses).

This paper illustrates, in particular, the estimation results and asymptotic analysis derived in [37], providing their numerically implementation from simulations. $L^2(\mathbb{M}_d, d\nu)$ -valued time series models, displaying different degrees of LRD, as well as SRD at different Jacobi frequencies are also analyzed here beyond any structural assumptions, opening a new research area.

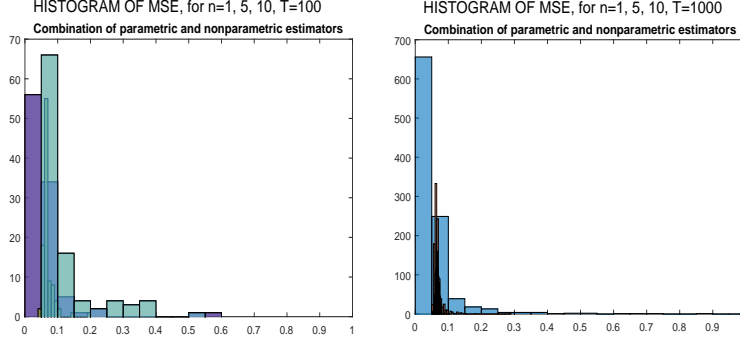


Figure 19: Histograms of the Empirical Mean Square Errors (EMSE) of $\hat{f}_\omega^{(T)} = \hat{f}_\omega^{(T, n_0)} + \hat{f}_\omega^{(T, (n_0+1, \infty))}$ at Legendre frequencies $n = 1, 5, 10$, based on a functional sample of size $T = 100$ (left-hand side) and of size $T = 1000$ (right-hand side). In the parametric part, minimization of the empirical contrast operator is achieved in the $\mathcal{L}(L^2(\mathbb{S}_2, d\nu; \mathbb{C}))$ operator norm.

Sections 5.1 and 5.2 illustrate this fact in a special case in a mixed parametric/nonparametric framework. A new battery of limit results is then required to derive the asymptotic analysis of the proposed estimators in this framework.

Note that, since the formulation of Theorems 4 and 5 in [28] is provided in a m -variate random field framework, the spectral analysis based approach presented here, for spatiotemporal wide sense stationary in time and isotropic in space random fields on compact and connected two-point homogeneous spaces, can be directly reformulated in the context of multivariate random fields. Particularly, alternative estimation approaches can be adopted in the approximation of the eigenvalues of the long-memory operator. That is the case of the Bayesian framework (see, e.g., [1] for the spherical random field case). The anisotropic framework will also be explored in a subsequent paper (see, e.g., [11], where a generalized Tikhonov regularization and reproducing kernel Hilbert space theory are applied, in the functional estimation of anisotropic covariance and autocovariance operators in the sphere).

Acknowledgements

This work has been supported in part by projects MCIN/ AEI/PGC2018-099549-B-I00, and CEX2020-001105-M MCIN/ AEI/10.13039/501100011033).

References

- [1] ALEGRÍA, A., BISSIRI, P.G., CLEANTHOUS, G., PORCU, E. and WHITE, P. (2021). Multivariate isotropic random fields on spheres: Non-parametric Bayesian modeling and L_p fast approximations. *Electronic Journal of Statistics* **15** 2360–2392.
- [2] ALEGRÍA, A. and CUEVAS-PACHECO, F. (2020). Karhunen–Loève expansions for axially symmetric Gaussian processes: modelling strategies and L^2 approximations. *Stoch Environ Res Risk Assess.* **34** 1953–1965.
- [3] ÁLVAREZ-LIÉBANA, J., LÓPEZ-PÉREZ, A., FEBRERO-BANDE, M. and GONZÁLEZ-MANTEIGA, W. (2022). A goodness-of-fit test for functional time series with applications to Ornstein-Uhlenbeck processes. Submitted manuscript, *arXiv:2206.12821*.
- [4] ANDREWS, G.E., ASKEY, R. and ROY, R. (1999). Special Functions. *Encyclopedia of Mathematics and its Applications*. Vol. **71**. Cambridge University Press, Cambridge.
- [5] ANH, V.V., BROADBRIDGE, P., OLENKO, A. and WANG Y.G. (2018). On approximation for fractional stochastic partial differential equations on the sphere. *Stoch Environ Res Risk Assess* **32** 2585–2603.
- [6] ANH, V., LEONENKO, N.N. and RUIZ-MEDINA, M.D. ((2016)). Space-time fractional stochastic equations on regular bounded open domains. *Fract. Calc. Appl. Anal.* **19**, 1161–1199.
- [7] ANH, V., LEONENKO, N.N. and RUIZ-MEDINA, M.D. (2016). Fractional-in-time and multifractional-in-space stochastic partial differential equations. *Fract. Calc. Appl. Anal.* **19** 1434–1459. DOI:10.1515/fca-2016-0074
- [8] BERAN, J. (2017). *Mathematical Foundations of Time Series Analysis*. Springer, Switzerland.
- [9] BOSQ, D. (2000). *Linear Processes in Function Spaces*. Springer, New York.
- [10] CAPONERA, A. (2021). SPHARMA approximations for stationary functional time series in the sphere. *Stat Infer Stoch Proc.* **24** 609–634.

- [11] CAPONERA, A., FAGEOT, J. SIMEONI, M. and PANARETOS, V.M. (2022). Functional estimation of anisotropic covariance and autocovariance operators on the sphere. *Electronic Journal of Statistics* **16** 5080–5148.
- [12] CAPONERA, A. and MARINUCCI, D. (2021). Asymptotics for spherical functional autoregressions. *Ann Stat* **49** 346–369.
- [13] CARTAN, E. (1927). Sur certaines formes Riemanniennes remarquables des géométries á groupe fondamental simple. *Ann. Sci. Éc. Norm. Supér.* **3** 345–467.
- [14] CLEANTHOUS, G., GEORGIADIS, AG., LANG, A. and PORCU, E. (2020). Regularity, continuity and approximation of isotropic Gaussian random fields on compact two-point homogeneous spaces. *Stoch Process Their Appl.* **130** 4873–4891.
- [15] CLEANTHOUS, G., PORCU, E. and WHITE, P. (2021). Regularity and approximation of Gaussian random fields evolving temporally over compact two-point homogeneous spaces. *TEST.* **30** 836–860.
- [16] DE LA CERDA, J.C., ALEGRÍA, A. and PORCU, E. (2018). Regularity properties and simulations of Gaussian random fields on the sphere cross time. *Electronic Journal of Statistics* **12** 399–426.
- [17] DURASTANTI, C. (2019). Aliasing effects for random fields over spheres of arbitrary dimension. *Electronic Journal of Statistics* **13** 3297–3335.
- [18] D’ OVIDIO, M., LEONENKO, N N. and ORSINGER, E. (2016). Fractional spherical random fields. *Statistics and Probability Letters.* **116** 146–156.
- [19] EMERY, X. and PORCU, E. (2019). Simulating isotropic vector-valued Gaussian random fields on the sphere through finite harmonic approximations. *Stoch Environ Res Risk Assess.* **33** 1659–1667.
- [20] GUILLAS, S. (2002). Doubly stochastic Hilbertian processes. *J Appl Probab.* **39** 566–580.
- [21] HÖRMANN, S. and KOKOSZKA, P. (2010). Weakly dependent functional data. *Ann. Statist.* **38** 1845–1884.
- [22] HORVÁTH, L. and KOKOSZKA, P. (2012). *Inference for Functional Data with Applications*. Springer, New York.

- [23] KARA-TERKI, N. and MOURID, T. (2016). Local asymptotic normality of Hilbertian autoregressive processes. *Comptes Rendus Mathématique*. **354** 634– 638.
- [24] KOKOSZKA, P. and REIMHERR, M. (2013). Determining the order of the functional autoregressive model. *J. Time Ser. Anal.* **34** 116–129.
- [25] LEONENKO, N. N., NANAYAKKARA, R. and OLENKO, A. (2021). Analysis of spherical monofractal and multifractal random fields. *Stoch. Environ. Res. Risk Assess.* **35** 681–701.
- [26] LI, D., ROBINSON, P.M. and SHANG, H.L. (2019). Long-range dependent curve time series. *J. of the American Statistical Association*. **115** 957–971.
- [27] LÓPEZ-PÉREZ, A., FEBRERO-BANDE, M. and GONZÁLEZ-MANTEIGA, W. (2021). Parametric estimation of diffusion processes: A review and comparative study. *Mathematics*. **9** 859.
- [28] MA, C. and MALYARENKO, A. (2020). Time varying isotropic vector random fields on compact two point homogeneous spaces. *J Theor Probab.* **33** 319–339.
- [29] MARINUCCI, D. and PECCATI, G. (2011). *Random fields on the Sphere. Representation, Limit Theorems and Cosmological Applications*. London Mathematical Society Lecture Note Series 389. Cambridge University Press, Cambridge.
- [30] MARINUCCI D., ROSSI M. and VIDOTTO A. (2020). Non-universal fluctuations of the empirical measure for isotropic stationary fields on $\mathbb{S}^2 \times \mathbb{R}$. *Ann Appl Probab.* **31** 2311–2349.
- [31] PANARETOS, V. M. and TAVAKOLI, S. (2013a). Fourier analysis of stationary time series in function space. *Ann. Statist.* **41** 568–603.
- [32] PANARETOS, V. M. and TAVAKOLI, S. (2013b). Cramér–Karhunen–Loève representation and harmonic principal component analysis of functional time series. *Stochastic Process and their Applications*. **123** 2779–2807.
- [33] PHAM, T. and PANARETOS, V. (2018). Methodology and convergence rates for functional time series regression. *Statistica Sinica*. **28** 2521–2539.
- [34] RAMM, A.G. (2005). *Random Fields Estimation*. Longman Scientific & Technical, Harlow.

- [35] RUBÍN, T. and PANARETOS, V. M. (2020a). Functional lagged regression with sparse noisy observations. *Journal of Time Series Analysis*. **41** 858–882.
- [36] Rubín, T. and Panaretos, V. M. (2020b). Spectral simulation of functional time series. arXiv preprint arXiv:2007.08458.
- [37] RUIZ–MEDINA, M. D. (2022). Spectral analysis of long range dependence functional time series. *Fractional Calculus and Applied Analysis*. **25** 1426–1458.
- [38] TAVAKOLI, S. (2014). *Fourier Analysis of Functional Time Series with Applications to DNA Dynamics*. Ph.D. dissertation, EPFL. Available at <http://dx.doi.org/10.5075/epfl-thesis-6320>.
- [39] TAVAKOLI, S. and PANARETOS, V. M. (2016). Detecting and localizing differences in functional time series dynamics: a case study in molecular biophysics. *Journal of the American Statistical Association*. **111** 1020–1035.